Progress in Oceanography 228 (2024) 103315

Contents lists available at ScienceDirect

Progress in Oceanography

journal homepage: www.elsevier.com/locate/pocean

Bioregionalization of the subarctic Pacific based on phytoplankton phenology and composition

Marta Konik [a,e,*], M. Angelica Peña [b], Toru Hirawake [c], Brian P.V. Hunt [d], Perumthuruthil Suseelan Vishnu [a,j,k], Lisa B. Eisner [f], Astrid Bracher [g,h], Hongyan Xi [g], Christian Marchese [a,d,i], Maycira Costa [a]

[a] University of Victoria, Victoria, BC, Canada
[b] Fisheries and Oceans Canada, Institute of Ocean Sciences, Sidney, BC, Canada
[c] National Institute of Polar Research, Tokyo, Japan
[d] University of British Columbia, Vancouver, BC, Canada
[e] Institute of Oceanology, Polish Academy of Sciences, Sopot, Poland
[f] National Oceanic and Atmospheric Administration, National Marine Fisheries Service, Alaska Fisheries Science Center, Seattle, WA, USA
[g] Alfred Wegener Institute, Helmholtz Centre for Polar and Marine Research, Bremerhaven, Germany
[h] Institute of Environmental Physics, University Bremen, Bremen, Germany
[i] European Molecular Biology Laboratory (EMBL), Monterotondo, Rome, Italy
[j] Department of Engineering Cybernetics, Norwegian University of Science and Technology, 7034 Trondheim, Norway
[k] Center for Autonomous Marine Operations and Systems, Norwegian University of Science and Technology, 7034 Trondheim, Norway

ARTICLE INFO

Keywords:
Ocean colour
Biogeochemical regions
Phytoplankton phenology
Self-Organized Maps
Subarctic Pacific Ocean

ABSTRACT

The subarctic Pacific is generally perceived as relatively homogeneous since the North Pacific Subpolar Gyre dominates the water circulation in the area. However, previous research showed significant spatial differences in phytoplankton abundance and community structure. This study aimed to identify regions associated with distinct phytoplankton phenology and composition to comprehensively describe the main phytoplankton variability patterns across the subarctic Pacific. To this end, satellite GlobColour time series observations and an extensive in situ phytoplankton pigment dataset were used in the analysis. Five bioregions were identified, based on the Self-Organized Mapping technique, using a greater than 20-year satellite data series. The bioregions in the open Pacific waters were dominated by green algae, haptophytes, and pelagophytes and were divided into the areas affected by the North Pacific Transition Zone and beyond. The other bioregions were defined around the Pacific basin margins where the diatom contribution was generally higher, with a particular distinction of waters surrounding the Kuril and the Aleutian Islands. Our bioregion designations allow for future evaluation of the processes controlling the physical and biological dynamics within each bioregion, which has direct implications for foraging conditions available to higher trophic levels, including potential food resource competition.

1. Introduction

The subarctic Pacific is one of the three main High Nutrient, Low Chlorophyll (HNLC) regions of the World Ocean due to low iron supply, which is the major factor suppressing its primary productivity (Nishioka et al., 2020). The primary producers in this region are a heterogeneous group including eukaryotes, such as diatoms, dinoflagellates, haptophytes, pelagophytes, prasinophytes, cryptophytes, chlorophytes, and much smaller but abundant picocyanobacteria, *Synechococcus* (Mochizuki et al., 2002; Booth et al., 1993). The composition of the phytoplankton community has implications for the balance between exported and recycled production (Vidussi et al., 2001; Laufkötter et al., 2013), as well as food web structure and production (Sommer et al., 2018; Rosengard et al., 2021; Zhang et al., 2021). In addition to phytoplankton abundance and composition, the seasonal cycle of phytoplankton production plays a key role in the food web through match/mismatch dynamics with zooplankton and knock-on effects to higher trophic levels (Hjort, 1926; Cushing, 1990; Suchy et al., 2022). This is particularly important considering the recently reported population declines of many fish species (Bendriem et al., 2019), including

* Corresponding author at: University of Victoria, Victoria, BC, Canada.
E-mail address: martakonik@uvic.ca (M. Konik).

https://doi.org/10.1016/j.pocean.2024.103315
Received 14 July 2023; Received in revised form 9 July 2024; Accepted 23 July 2024
Available online 26 July 2024

the ecologically, culturally, and economically important Pacific salmon (Burger et al., 2015). Due to their anadromous nature, understanding salmon declines is challenging, as multiple factors across different freshwater and marine habitats can affect the status of their populations (Honkanen et al., 2019). Although salmon survival during their first year at sea is considered to be critical to returning success (McKinnell and Irvine, 2021; Claiborne et al., 2021), the role of salmon's life history experience in the open ocean in successful returns remains a major knowledge gap (Chittenden et al., 2009; Myers et al., 2016). Characterizing spatial and temporal changes in phytoplankton phenology and composition at the base of the food web in this region is, therefore, an important step towards estimating potential environmental pressures on fish stocks, including Pacific salmon (Myers et al., 2016).

The timing of phytoplankton bloom initiation and seasonal changes in biomass, also called phytoplankton phenology (Isles and Pomati, 2021), has been characterized by chlorophyll-*a* concentration (Chl-*a*) fluctuations over time, using a variety of phytoplankton phenology metrics at relatively small geographical scales (Krug et al., 2018; Lavigne et al., 2018; Suchy et al., 2022). This characterization across large ocean basins such as the subarctic Pacific is challenging, thus requiring some form of subdivision, which is often based on, for example, hydrological patterns (Liu et al., 2004; Peña et al., 2019) and related to surface Chl-*a* (e.g., Platt and Sathyendranath, 1988). One of the first definitions of oceanic ecological regions based on ocean primary productivity (PP) was completed using satellite-derived Chl-*a* from the Coastal Zone Color Scanner (CZCS) in the Atlantic Ocean (Platt and Sathyendranath, 1988). Following this work, Longhurst et al. (1995) used satellite-derived Chl-*a* to partition the entire Global Ocean's pelagic environment into bioregions, which became a benchmark (UNESCO, 2009). Subsequently, bioregionalization of individual oceans and seas has been established to analyze their spatial variability in more detail using regional Chl-*a* products (Hilborn and Devred, 2022; Marchese et al., 2019; Marchese et al., 2022), PP (Feng et al., 2022), phytoplankton and zooplankton taxonomic composition (Kléparski et al., 2021), and carbon fluxes (Ciavatta et al., 2019).

The structure of marine ecosystems has also been described using numerical models based on, for example, nutrients, phytoplankton, zooplankton, and detritus (NPZD), which further developed the demand for information about the phytoplankton functional types (PFT), such as diatoms or picophytoplankton (Anderson, 2005). The potential of using the marker pigments' light absorption properties for distinguishing PFT was reported by Alvain et al. (2005), by exploiting the relationship between the phytoplankton pigments and water-leaving radiance using modern ocean colour satellites with high spectral resolution which allows for the detection of subtle changes in spectral shapes (Alvain et al., 2005; Alvain et al., 2008; Hirata et al., 2008). The study by Le Quéré et al. (2005) presented further correspondence between the PFT and phytoplankton size classes (PSC), which many researchers have used to link PFT and PSC with diagnostic pigments (e.g., Hirata et al., 2011; Moisan et al., 2017; Chase et al., 2020; Xi et al., 2020), summarized in a review by Mouw et al. (2017) and Bracher et al. (2017). However, the satellite-based distinction between PFT is challenging because pigments are shared among several different taxa (Gieskes et al., 1988; Wright and Jeffrey, 2005; Jeffrey and Wright, 2006). A way to overcome this problem is the method adopted by Vishnu et al. (2022), who derived *in situ* PFT estimates from the chemotaxonomic analysis (CHEMTAX) (Mackey et al., 1996), allowing for the identification of particular taxa based on *a priori* knowledge of the pigment characteristics within each group (Wright and Jeffrey, 2005).

In this study, we aimed to define bioregions within the subarctic Pacific as a first step towards better characterizing the spatial and temporal variability of phytoplankton phenology and associated composition. Historical measurements of pigment composition were compiled, along with recent data collected in the scope of the International Year of the Salmon (IYS) High Seas Expeditions. These data were used to evaluate existing satellite-based algorithms of PFT based on the GlobColour merged ocean colour satellite data series (ACRI-ST et al., 2017). The satellite data were subsequently used to derive phytoplankton phenology and PFT data series of 20+ years to identify distinct bioregions using the machine-learning technique of Self-Organized Mapping (SOM) (Kohonen, 2013). The novel bioregionalization revealed the subtle variability of phytoplankton spatial dynamics in the subarctic Pacific, which can be further used as spatial units for monitoring response to climate change and associated environmental conditions for zooplankton, Pacific salmon, and other pelagic fish and nekton in this region.

2. Methods

2.1. Study area

The bioregionalization was restricted to the open waters of the subarctic Pacific, covering salmon's feeding grounds during the marine life stage (Graham et al., 2020; McKinnell and Irvine, 2021) (Figure S1). The study area is delineated in the east by North America and in the west by northern Japan, the Kuril Islands, and the Siberian coast with the Kamchatka Peninsula. The coastal areas within the 500-m isobath (GEBCO, 2022) (Fig. 1) were excluded from the analysis to minimize the influence of the land runoff that changes the optical water properties and dominates variability (Phillips and Costa, 2017; Mizuno et al., 2018; Giannini et al., 2021). We also limited the study area in the north to the natural barrier of the Aleutian Archipelago that separates the oceanographically distinct Bering Sea (Stabeno et al., 1999). The southern border, at 40°N, follows the northern front of the North Pacific Transition Zone (NPTZ), an area of gradual mixing of cooler and less saline subarctic waters with warmer saline subtropical waters. The NPTZ stretches between 32°N and 42°N and fluctuates latitudinally by about 10° yearly (Roden, 1991). The NPTZ outlines the gradient in surface Chl-*a* concentrations, called the transition zone chlorophyll front (TZCF), operationally defined as the 0.2 mg m^{-3} contour (Ayers and Lozier, 2010), and has been identified as a primary migration pathway and foraging ground for marine predators due to a strong convergent flow capable of concentrating zooplankton (Polovina et al., 2001). The subarctic waters on the northern side of NPTZ are more abundant in nutrients compared to subtropical waters (Ayers and Lozier, 2010), and due to a lack of iron in the euphotic layer, this region is an HNLC zone (Nishioka et al., 2021). The phytoplankton abundance is controlled by the strong winds transporting iron-rich dust from Asian deserts, as well as the top-down zooplankton grazing (Strom and Welschmeyer, 1991; Tsuda et al., 2007).

2.2. Data set

Satellite-derived phytoplankton phenology and community composition were the primary data used in the bioregionalization of the subarctic Pacific (Fig. 2). The phenology was retrieved from the merged ocean colour satellite data provided in the GlobColour Chl-*a* data set (ACRI-ST et al., 2017), and the community composition was derived using *in situ* pigment measurements that were converted into locally-tuned GlobColour-derived PFT data series following the study by Xi et al. (2021). The final bioregions were obtained using the SOM clustering approach (Kohonen, 2013).

2.2.1. In situ HPLC data set

The original *in situ* dataset comprised of HPLC samples collected during the IYS cruises in 2019, 2020, and 2022, and several open-access datasets such as Nomad, MAREDAT, SGLI/GCOM-C, the longest Canadian time series of measurements along Line-P, and west of Vancouver Island (Table 1), adding up to 1,182 samples in total.

The 2022 *in situ* data set consisted of 89 samples collected between February and April as part of the IYS initiative (https://yearofthesalmon.org/2022expedition/). Since the sampling area was mainly

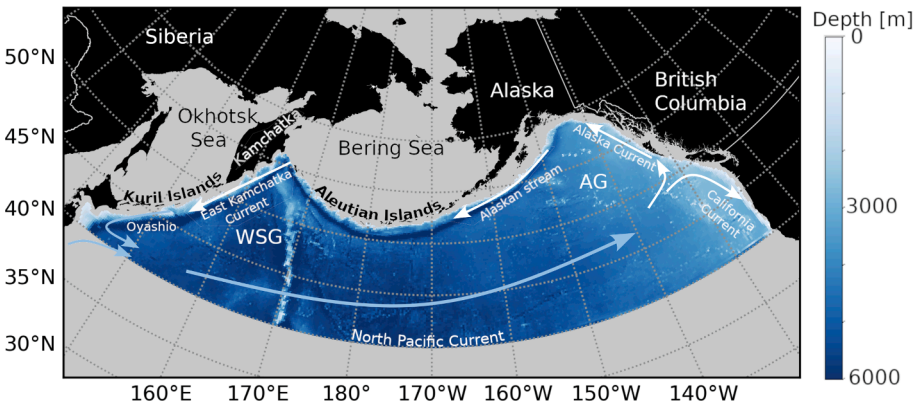

Fig. 1. Map of the bottom topography (GEBCO, 2022) limited to the study area, overlaid with a general view of the major currents; AG – Alaskan Gyre, WSG – Western Subarctic Gyre.

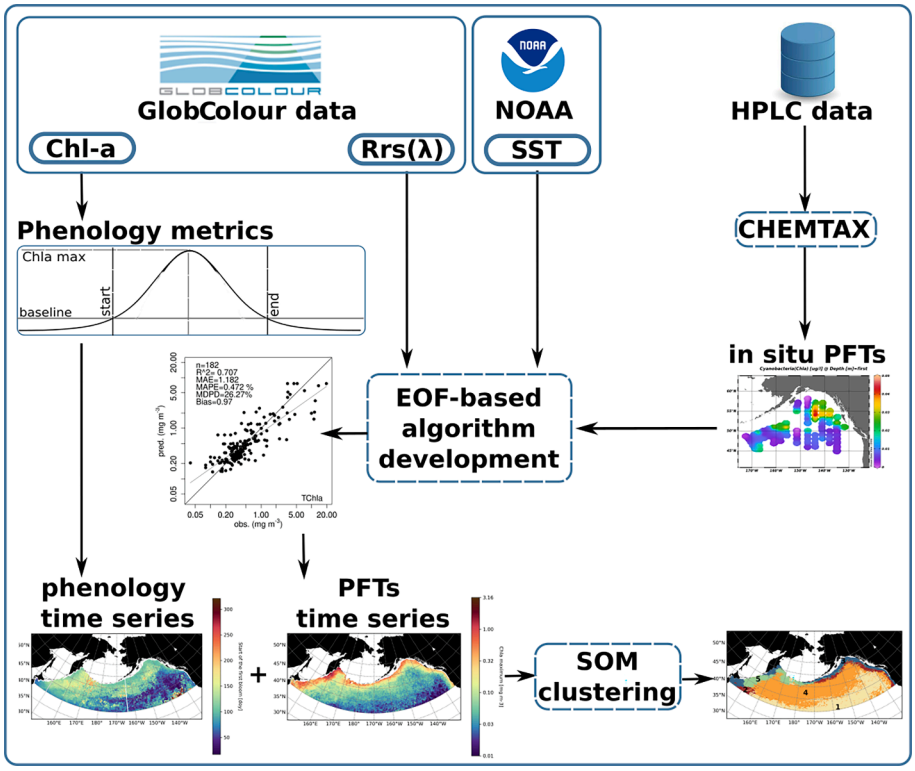

Fig. 2. Diagram of the workflow to derive bioregions.

within the HNLC zone (Goes et al., 2004; Sasaoka et al., 2011), we adopted the filtering "to colour" sampling protocol, meaning the filtered volume was sufficient to macroscopically observe a change in the filter's colour (Nemcek and Peña, 2014). At each station, duplicate water samples were collected at 5 m depth using Niskin bottles mounted on a rosette and filtered under a low vacuum (<200 mm Hg/vac) through 25 mm diameter Whatmann GF/F filters. The filters were flash-frozen and stored at –80 °C until the High-Performance Liquid Chromatography (HPLC) analyses were conducted at the Belle W. Baruch Institute for Marine and Coastal Sciences, University of South Carolina (USC), USA, according to the method by Pinkney (2010). In addition, flow cytometry samples for counts of phytoplankton cells were collected in 2022, at the same stations and depths (Eisner and Lomas, 2022), to validate the retrieved phytoplankton groups.

The data set from the IYS sampling campaign was expanded by records extracted from open-access databases to provide sufficient geographic coverage for the satellite model development (Table 1; the monthly and yearly data distributions are presented in the supplement, Figure S2). Only samples collected at 6 m depth or shallower were used to ensure comparability with the satellite ocean colour measurements (Brewin et al., 2015). As in the clearest surface ocean waters the total Chl-*a* concentration is generally between 0.01 – 0.02 mg m^{-3} (Morel et al., 2007), the stations where the total Chl-*a* (total Chl-*a* = chl-*a* + DVchl *a* + chlide *a* + chl *a* allomers and epimers) was below 0.01 mg m^{-3} were excluded from the analysis, and individual pigment concentrations that did not exceed 0.001 mg m^{-3}, which was the detection limit, were reset to 0 (Uitz et al., 2006; Pinkney, 2010).

2.2.2. *Satellite-based Chl-a phenology and PFT*

The phytoplankton phenology and PFT were derived from 8-day Level-3 25 km products obtained from the GlobColour project (ACRI-ST et al., 2017; last accessed: 2023–02-24), which combined SeaWiFS (1997–2010), MERIS (2002–2012), MODIS-Aqua (2002-present), VIIRS-NPP (2012-present), and VIIRS-JPSS-1 (2017-present). The CHL1 AVW

Table 1
List of data sources and references to the HPLC pigment data sets used in this study.

Data source	Reference
IYS 2022	*this paper*
IYS 2019 and 2020	Vishnu and Costa, 2023
Line-P	Peña et al., 2019
	Department of Fisheries and Oceans – Canada (https://open.canada.ca/data/en/dataset/871b0b32-3135-40c8-868e-c5d87800ca76)
West Coast Vancouver Island data	*Department of Fisheries and Oceans – Canada (https://open.canada.ca/data/en/dataset/61877f60-1a1e-4c3d-8a28-02fdf071e5a8)*
MAREDAT	Peloquin et al., 2013; Letelier, 2007; Head, 2002; Hayakawa et al., 2008; Suzuki et al., 2002b
SGLI/GCOM-C	Waga et al., 2022
SeaBASS	Werdell et al., 2003, *https://doi.org/10.5067/SeaBASS/VIMS_2005/DATA001*
Nomad v2a	*Werdell and Bailey, 2006*

product based on the algorithms designed for the case-1-waters (O'Reilly and Werdell, 2019) was used to determine the phenology metrics starting in January 1998 (Pramlall et al., 2023; Welch et al., 2020). From the same GlobColour data set, the remote sensing reflectance (R_{rs}) products in nine spectral bands centred at 412, 443, 469, 490, 531, 555, 645, 670, and 678 nm were used in the PFT model development. To produce a homogeneous PFT time series, only data from 2002 to 2022 and with the nine bands were used in this analysis because, before the year 2002, the ocean colour satellites had limited bands available. Additionally, Sea Surface Temperature (SST) daily maps at 0.25°x0.25° NOAA OISST v2 high-resolution data (Reynolds et al., 2002; Reynolds et al., 2007) provided by the NOAA/OAR/ESRL PSL, Boulder, Colorado, USA (NOAA, 2007) were included in the PFT algorithm following Xi et al. (2021).

2.2.2.1. Deriving phytoplankton phenology. Computation time was optimized by selecting a 25-km spatial resolution, which successfully represents the variability across the subarctic Pacific and minimizes missing data (Figure S3). Residual data gaps were dealt with in two distinct manners: (i) pixels with more than 60 % of missing values within the entire time series were excluded, and (ii) to all the other missing pixels, linear interpolation in time was applied to every pixel on a year-by-year basis, where the extreme months, January and December, were not interpolated even when values were missing (Brody et al., 2013). The yearly interpolation approach was adopted based on the assumption of no blooms starting in December or January due to light-limiting conditions north of 40°N. For these months, bloom-like increases in Chl-*a* have been reported in the literature, but they were found to result from the photoadaptation of phytoplankton and not an increase in biomass (Wilson and Coles, 2005; Yoo et al., 2008). With a spatially continuous time series, the yearly data were smoothed using a three-point median filter following Lavigne et al. (2018).

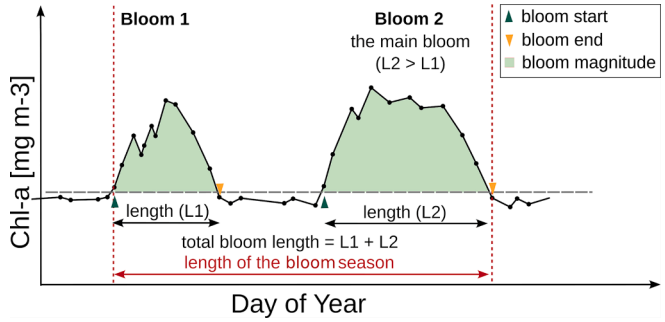

Fig. 3. Schematic representation of the phenology metrics used in this study.

The following step was to define phytoplankton phenology metrics (Fig. 3), starting with the bloom timing. This was recognized when a pixel-specific Chl-*a* value exceeded a predetermined Chl-*a* baseline threshold for at least two consecutive weeks to avoid classifying incidental peaks as blooms (Soppa et al., 2016; Krug et al., 2018; Suchy et al., 2022). The Chl-*a* baseline threshold corresponded to a value of 5 % above the climatological Chl-*a* median (Racault et al., 2012). Further, based on a median timeline extracted from a 3x3 pixel window (Okamoto et al., 2010), the following phenology metrics were determined (Fig. 3): (1) bloom start, meaning the day when Chl-*a* exceeded the baseline for at least two consecutive weeks, with a particular emphasis on the first bloom every year; (2) bloom end, which was the following date (expressed as Day of Year, DOY) of the drop in Chl-*a* below the baseline; (3) bloom length (expressed as the number of days), derived as the difference between the end and the start of each bloom; (4) maximum Chl-*a* concentration during each bloom; and (5) the date (DOY) when it occurred (Soppa et al., 2016; Krug et al., 2018). Next, (6) the number of blooms in every year was determined; (7) the total bloom length was computed by summing all days between the beginning and end of each bloom (Krug et al., 2018); and (8) the bloom magnitude was estimated by adding together Chl-*a* values during the bloom intervals, after Soppa et al. (2016). Additionally, (9) the length of the bloom season (number of days) was defined as the time elapsed between the start of the first bloom and the end of the last bloom, and the main bloom of the longest duration was determined (Fig. 3).

2.2.2.2. Deriving PFT maps. Producing the satellite-based PFT data series required a three-step approach. First, the *in situ* PFT groups were estimated by converting the HPLC pigment information, which varies depending on the within-group taxa composition, into the abundance (in Chl-*a* concentration) of each phytoplankton group using the CHEMTAX software (Mackey et al., 1996). Since estimating the contribution of each group to the overall phytoplankton community is an under-determined mathematical problem with an infinite number of factorizations (Mackey et al., 1997), providing a first-guess (initial) pigment ratios matrix is essential to determine expected phytoplankton groups. The expected groups and lineages (Supplement Table S1) and their pigment ratios were identified based on the literature (Table S2, Jeffrey and Wright, 2006; Zapata, 2005). Since our input CHEMTAX data consisted of *in situ* HPLC pigment samples collected between 1998 and 2022 (Figure S4) across the entire North Pacific Ocean (Table 1), set to address the main objective, we considered many factors that may have affected the phytoplankton pigment concentration ratios. For instance, the eastern and western parts of the subarctic Pacific show significant differences in the observed phytoplankton species, nutrient distributions, and physical water properties (Suzuki et al., 2002a). These differences may result in variability of the pigment concentration ratio due to, for example, different responses to environmental stress, such as iron limitation (Wright and Jeffrey, 2005; Takeda, 2011; Schuback et al., 2015). Moreover, older HPLC methods did not identify some of the pigments (Wright and Jeffrey, 2005), for example, lacked resolution of Chl-c_1/c_2 and some of the monovinyl and divinyl chlorophyll pairs, including the Chl-c_3 forms (Wright et al., 1991; Wright and Jeffrey, 2005). To minimize the uncertainty related to the east–west differences in pigment concentration ratios and address the HPLC limitations, we tested two input matrices: (Suzuki et al., 2002b), representing the western Pacific, and Peña et al. (2019), representing the eastern Pacific Ocean (Table S3). It is worth noting that both of these studies identified the same phytoplankton groups (cyanobacteria, chlorophytes, cryptophytes, diatoms, dinoflagellates, haptophytes, pelagophytes, and prasinophytes; Table S2) but described them using a few different pigments, which were, however, all included in the documentation of the CHEMTAX as definite pigments for each of those groups (Mackey et al., 1997; Wright and Jeffrey, 2005). The HPLC pigment data set was subsequently clustered based on the normalized values of the key pigment ratios

described by Higgins et al. (2011). These included the relative concentrations of chl-c_3 to total Chl-*a*, the sum of the chl-c_1, chl-c_2, peridinin, prasinoxanthin, fucoxanthin, 19′-hexanoyloxyfucoxanthin, 19′-butanoyloxyfucoxanthin, lutein, zeaxanthin, violaxanthin, alloxanthin, and Chl-*b*, and the ratios of zeaxanthin to lutein, and lutein to Chl-*b*. The clusters were derived based on the Hierarchical Agglomerative Clustering (HAC) using the 'ward.D2′ method with the Euclidean distance (Charrad et al., 2014; Murtagh and Legendre, 2014). This method was chosen because it operates in the multivariate Euclidean space, similar to the empirical orthogonal functions (EOF) approach also used for the satellite PFT model derivation (Murtagh and Legendre, 2014; Xi et al., 2020). The final number of clusters was determined using the Silhouette index, which estimates the average distance between points within the same cluster in reference to the average distance to the points in the neighbouring clusters (Rousseeuw, 1987; Mamat et al., 2018). This analysis resulted in seven clusters, and we tested each of them individually using the input matrices of Suzuki et al. (2002b) and Peña et al. (2019) (Supplement, Figure S4). Each time, 60 CHEMTAX trials were run, starting with the initial matrix modified by a factor $F = 1 + S * (R - 0.5)$, where R was a random number between 0 and 1, and S was a scaling factor of 0.7 (Mackey et al., 1997). The six best results were averaged for estimating the *in situ* PFT abundances, following methods by Peña et al. (2019). To assess this approach, we considered firstly the lower output CHEMTAX's group variability (Table S5), and secondly, and more importantly, we validated the output phytoplankton group Chl-*a* against the independent *in situ* flow cytometry dataset (Eisner and Lomas, 2022).

In the second step, the derived *in situ* PFT were used to produce the satellite-based PFT. Considering the spectral limitations of the satellite images, an additional clustering of the pigment concentrations was performed following methods by Kramer and Siegel (2019) and Vishnu et al. (2022) to identify the major phytoplankton groups and merge the least distinct groups obtained from the CHEMTAX analysis (Figure S5). The HAC clustering was applied to the pigments, and the main division threshold was adopted at the height of 40 considering the *a priori* pigment information, producing the six final phytoplankton groups: alloxanthin and zeaxanthin both clustered individually, showing distinct 1) cryptophytes and 2) cyanobacteria groups (Figure S5). A combination of fucoxanthin and the sum of chl-c_1 and c_2 indicated 3) diatoms (Peña et al., 2019). Lutein and Chl-*b* clustered together, suggesting a close connection between chlorophytes and prasinophytes, which were merged into one group of 4) green algae as in Xi et al. (2021). Peridinin indicated a distinct group of 5) dinoflagellates, despite the presence of prasinoxanthin and violaxanthin, suggesting a possible small input from prasinophytes-3 (Suzuki et al., 2002b; Peña et al., 2019). Finally, 19′-hexanoyloxyfucoxanthin was a major pigment in haptophytes, 19′-butanoyloxyfucoxanthin in pelagophytes, and chl-c_3 overlapped in both, therefore, 6) haptophytes and pelagophytes were also considered together (Kramer and Siegel, 2019). As a result, satellite algorithms were developed for the six phytoplankton groups shown in Figure S5: cryptophytes, cyanobacteria, diatoms, dinoflagellates, green algae, and hapto-pelago group.

As a third step, the EOF-based PFT model was used following methods by Xi et al. (2021). The final *in situ* PFT values below 0.005 mg-chl m^{-3} were additionally filtered, following Xi et al. (2021), and the satellite SST and R_{rs} matchups were extracted using 3x3 pixel windows where at least 50 % + 1 pixel within each window contained valid information (Bailey and Werdell, 2006). All the pixels beyond the range $< \mu–1.5\sigma, \mu + 1.5\sigma >$ (applied to $\log_{10}$-transformed $R_{rs}(\lambda)$ data, where μ and σ are the mean and the standard deviation, respectively) were excluded, along with values where the coefficient of variation (CV) exceeded 0.2 within the pixel window (Concha et al., 2021), which provided 182 final records. Subsequently, a covariance matrix C was computed based on the $R_{rs}(\lambda)$ spectra, and the singular value decomposition (SVD) was applied. Three matrices were produced: a diagonal matrix D with singular values, a V matrix containing the identified $R_{rs}(\lambda)$ patterns, and a U matrix with the coefficients ensuring reconstruction of the initial spectra (Golub and Kahan, 1965), but only significant patterns with singular values exceeding 0.01 % of the highest values were used (Xi et al., 2020). The generalized linear models (GLM) were implemented to determine the relationships between the *in situ* PFT $\log_{10}$–transformed Chl-*a* concentrations and SST, and the final coefficients resulting from the multiplication of matrices U and D. The GLM implemented as the *glm* function in *R* were used, with stepwise optimization of the number of variables number using the *step* function (R Core Team, 2018; Wickham, 2016; Wickham et al., 2019) and the Akaike information criterion (AIC) as the primary optimization measure (Hastie and Pregibon, 1992; Burnham et al., 2011). The GLM with the smallest change of the AIC was selected and assessed based on non-parametric measures such as the Root Mean Squared Logarithmic Error (RMSLE), the Median Absolute Percentage Error (MAPE), the Median Percent Difference (MDPD) applied to $\log_{10}$–transformed Chl-*a* and $R_{rs}(\lambda)$ values, the Mean Absolute Error (MAE), the coefficient of determination (R^2), and bias (Pahlevan et al., 2020). To ensure robustness, models were additionally assessed by generating 500 random training and test subset pairs in proportion 80/20 (Xi et al., 2020; Wong, 2015), and the overall cross-validation R^2, RMSLE, and MDPD statistics were determined (Table S6). The final models were applied to produce a complete series of PFT maps using the 9 GlobColour R_{rs} bands and the NOAA SST maps of similar temporal and spatial resolutions as the input GlobColour R_{rs} products, which were then used as inputs for the bioregionalization.

2.3. Identifying bioregions

The bioregions were identified following a two-level classification. In the first step, an artificial neural network based on Kohonen maps implemented in *R* (Wehrens and Buydens, 2007; Boelaert et al., 2021), called self-organizing maps (SOM) (Kohonen, 2013), was used. The SOM approach transforms multi-dimensional data into two dimensions, following one of the non-linear dimensionality reduction (NLDR) techniques (Lee and Verleysen, 2007). The topology of the data is represented discretely, usually by a lattice, where each node is a vector characterized by multiple weights that refer to the input variables. These weights are iteratively modified to reflect the distance between the nodes, considering their similarity while preserving the lattice's cohesion (Kohonen, 2013). Therefore, the SOM's shape, described by the similarity-related distance measure, the lattice size, and the neighbourhood type, severely affect the classification's results. This study used the hexagonal lattice as it does not favour any direction and tends to outcompete the rectangular ones (Brugger et al., 2008; Marchese et al., 2022). As the distance metric, the widely used Euclidean distance was selected since we investigated a continuous water body, and the primary contraindication is the existence of obstacles or natural barriers (Rathbun, 1998). Lastly, the initial number of SOM nodes was estimated at 29 x 29 nodes, following Elizondo et al. (2021), and the optimal size was selected by running SOM of the consecutive dimensions ranging between 5 x 5 and 45 x 45, and comparing the quantization error (QE), the topographic error (TE), their sum called the total error (TotE), and the explained variance, as suggested by Marchese et al. (2022). The size of 40 x 40 was optimum as TotE was the smallest and started to grow when the size increased, whereas the explained variance changed by less than 0.5 % (Figure S6). Based on the same approach of gradation followed by error-based assessment of each step, we established the parameters defining the neighbourhood properties, including the neighbourhood's radius affected during one iteration of 1.6, the adjustment factor α of 0.0001, and the iterations number of 700 (Wehrens and Buydens, 2007).

In the next step, the SOM nodes were classified (Vesanto and Alhoniemi, 2000) following an altered version of the K-means classification algorithm called the Partitioning About Medoids (PAM) (Reynolds et al., 2004). The Euclidean distance was used again as the distance metric. Since the PAM algorithm requires a predetermined number of clusters as

input parameters, the optimum number of clusters representing bioregions was established by testing division into 2 and progressing up to 35, recording the Silhouette index every time. Lastly, the significance of the differences between bioregions was investigated using the Kruskal-Wallis test, a non-parametric alternative for the one-way analysis of variance (ANOVA), where the null hypothesis assumes measurements from all the subsets stemming from a common distribution. This analysis was followed by a pairwise *post hoc* Dunn's test with implemented Bonferroni adjustment (Dinno, 2015), which was used previously by other authors to compare ecoregions (Fendereski et al., 2014; Marchese et al., 2022).

3. Results

The results are presented as follows: (i) an overview of the phytoplankton phenology across the subarctic Pacific, (ii) estimation and evaluation of the derived PFT, and (iii) the bioregionalization obtained, with comparison among bioregions.

3.1. Phytoplankton phenology

The retrieved climatology-based spatial variability showed that the study area was characterized by low Chl-*a* (<0.5 mg m^{-3}) in the subarctic Pacific basin, with maximum Chl-*a* values around the basin continental margins, particularly pronounced west of Japan and Kamchatka (>3 mg m^{-3}; Fig. 4h). Two blooms dominated the annual cycle across the subarctic Pacific with only a few exceptions (Fig. 4b). One bloom was observed near southern British Columbia (BC) and the western Aleutian Islands, while three blooms were observed along the northernmost position of the NPTZ. In areas associated with one bloom per year, these generally started in the second half of the year, whereas elsewhere, blooms began in the first half of the year (Fig. 4a). The earliest first blooms occurred around February in the southeastern part of the study area, between 40°N and 50°N. The first bloom timing was generally later (March-May) in the northeast and western parts of the study area and in the central Pacific. Around Japan and the west of BC, the first bloom's onset was observed in late March (between the 73rd and 83rd DOY). Further north, on the coast of Alaska and the Aleutian Archipelago, the start of the first bloom was delayed by about a month

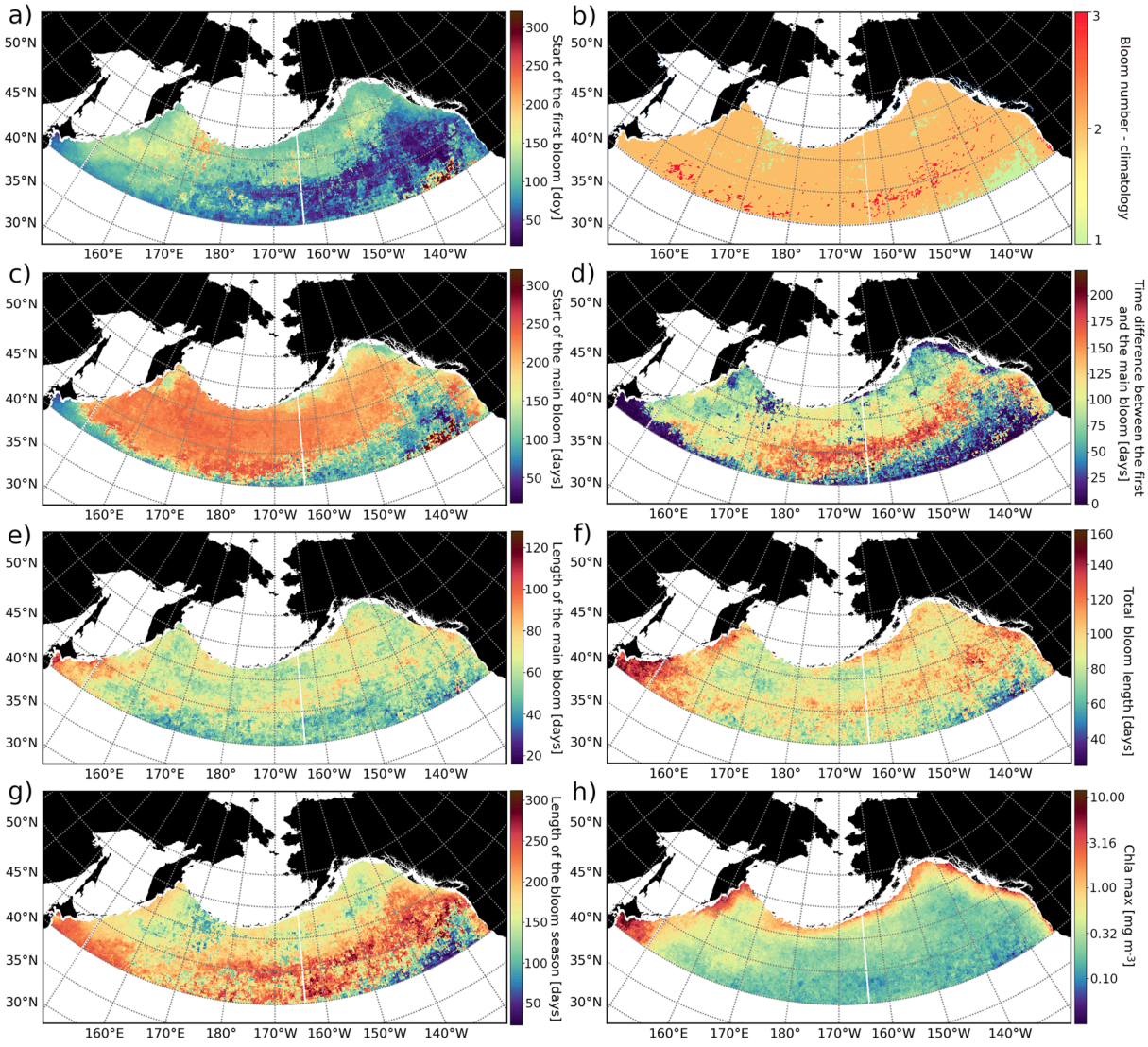

Fig. 4. Maps of the primary phenology metrics calculated from the Chl-*a* climatology (1998 – 2022): a) start of the first bloom [Day Of Year], b) number of blooms, c) start of the main (the most prolonged) bloom [Day Of Year], d) time difference between the start of the first and the main bloom [days], e) length of the main bloom [days], f) total bloom length [days], g) length of the bloom season (time between the start of the first bloom and the end of the last one) [days], and h) Chl-*a* maximum value during the main bloom [mg m^{-3}].

(between the 105th and 133rd DOY), similar to regions close to the Kamchatka Peninsula. The latest first blooms were observed in July (between the 180th and 200th DOY), southwest of the Aleutian Archipelago, where the deepest passages are located (170°E – 175°E), partly co-occurring with the northernmost areas limited to one bloom per year (Fig. 4b).

The main bloom started primarily after June (Fig. 4c), except for a few areas in the southeastern region and along the southern border of the subarctic region at 40°N. A pronounced difference between the start of the first and main blooms was observed in the central Pacific, along the 45°N parallel (Fig. 4d). In the north, the time gap between these blooms decreased due to the later onset of the first bloom, indicating the primary role of light limitation on phytoplankton growth. The main bloom was typically the longest (>3 months) east of Japan and the southern Kuril Islands (Fig. 4e) and ~ 3 months long in the waters southwest of BC, southeast of the Aleutian Archipelago, and across the Pacific, between 45°N and 50°N. In other areas, the main bloom lasted for 40–60 days. The total bloom length followed a similar pattern to the main bloom, with even more pronounced long bloom conditions around Japan and BC (Fig. 4f).

The period between the start of the first bloom and the end of the last bloom was also computed as a rough estimate of the duration of the

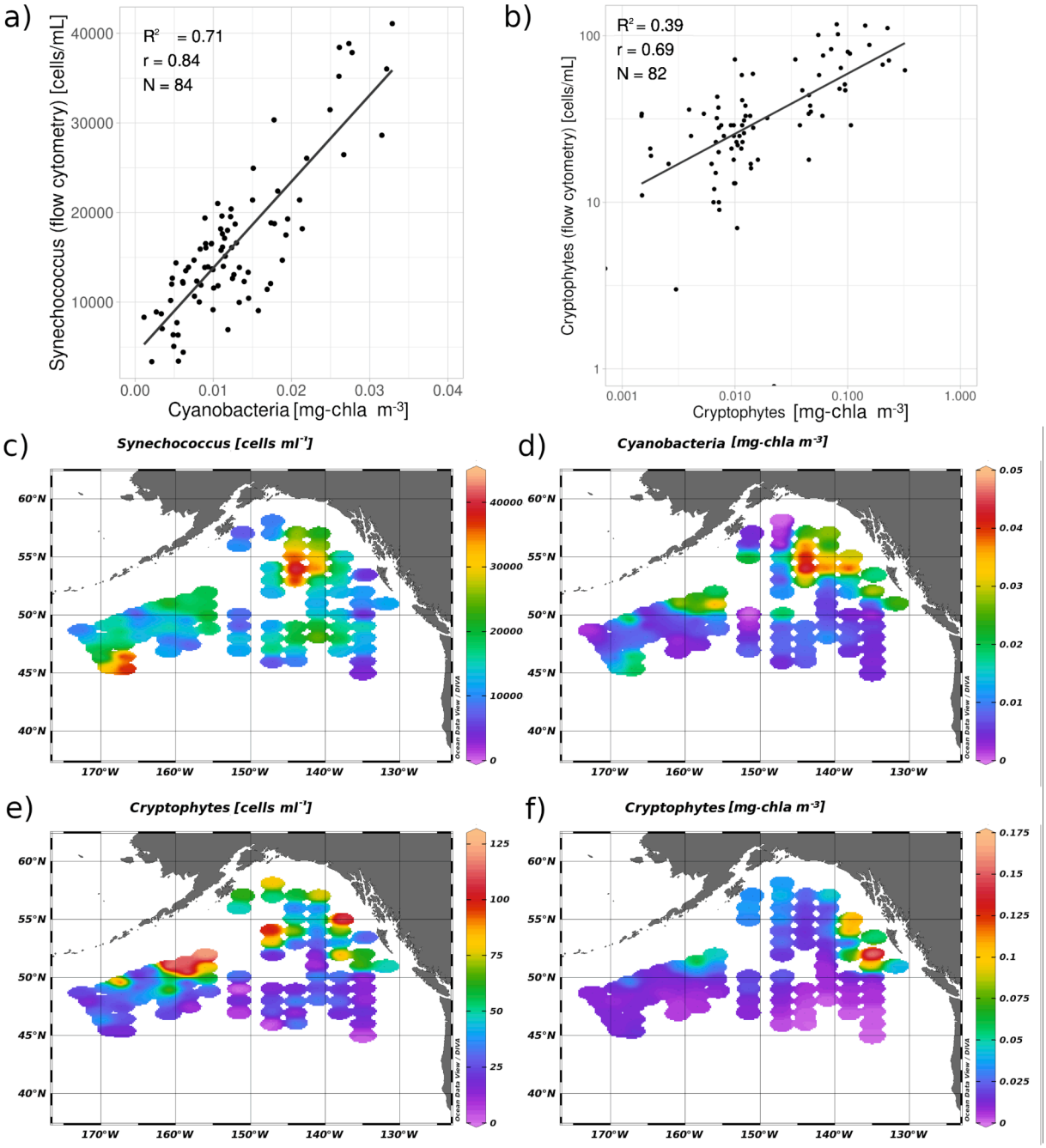

Fig. 5. Comparison of: a) CHEMTAX-derived cyanobacteria Chl-*a* concentration [mg-chl m^{-3}] and flow cytometry–derived *Synechococcus* spp. cell counts [cells ml^{-1}], b) CHEMTAX-derived cryptophytes Chl-*a* concentration [mg-chl m^{-3}] and flow cytometry–derived cryptophytes cell counts [cells ml^{-1}], and the surface distributions of c) *Synechococcus* spp. cell counts, d) CHEMTAX-derived cyanobacteria Chl-*a* concentration [mg-chl m^{-3}], e) cryptophytes cell counts [cells ml^{-1}], and f) CHEMTAX-derived cryptophytes Chl-*a* concentration [mg-chl m^{-3}]. The r and R^2 were estimated for the log_{10}–transformed b) cryptophytes values. The Data-Interpolating Variational Analysis (DIVA) implemented in the Ocean Data View software (Schlitzer, 2021) were used in c, d, e, and f.

bloom season (Fig. 4g). Across most of the southern subarctic Pacific, the bloom season started in February and lasted until November. In the northernmost regions, the bloom season was shorter (Fig. 4g), even in the areas associated with two blooms (Fig. 4b). The shortest bloom season was found in the single-bloom regions southwest of the Aleutian Islands (Fig. 4g).

3.2. Phytoplankton functional types

3.2.1. Validation of the CHEMTAX output

Similar to Fujiki et al. (2009), the CHEMTAX output was verified by assessing the stability between the six best CHEMTAX runs (Table S5) and comparing its output with the *in situ* flow cytometry samples. The variability among the resulting marker pigments for each of the final groups (cyanobacteria, cryptophytes, diatoms, dinoflagellates, chlorophytes, prasinophytes, haptophytes and pelagophytes) did not exceed 40 %. Further, the relative contribution of each group to total Chl-*a* varied up to 31 %, which was within the limit recommended by Mackey et al. (1997). The CHEMTAX cyanobacteria group was limited to one of the two main genera, *Synechococcus*, identified using zeaxanthin (Suzuki et al., 2002b; Peña et al., 2019). The other one, *Prochlorococcus,* is generally considered absent in the subarctic Pacific waters (Liu et al., 2002; Zhang et al., 2008), and in our data set, its marker pigment was seen in small amounts at only a few stations around Line-P, which suggested a possible intrusion of subtropical waters due to the NPTZ shifting northwards (Suzuki et al., 2005).

A comparison of the CHEMTAX cyanobacteria output to the *in situ* flow cytometry samples for *Synechococcus* spp. showed a statistically

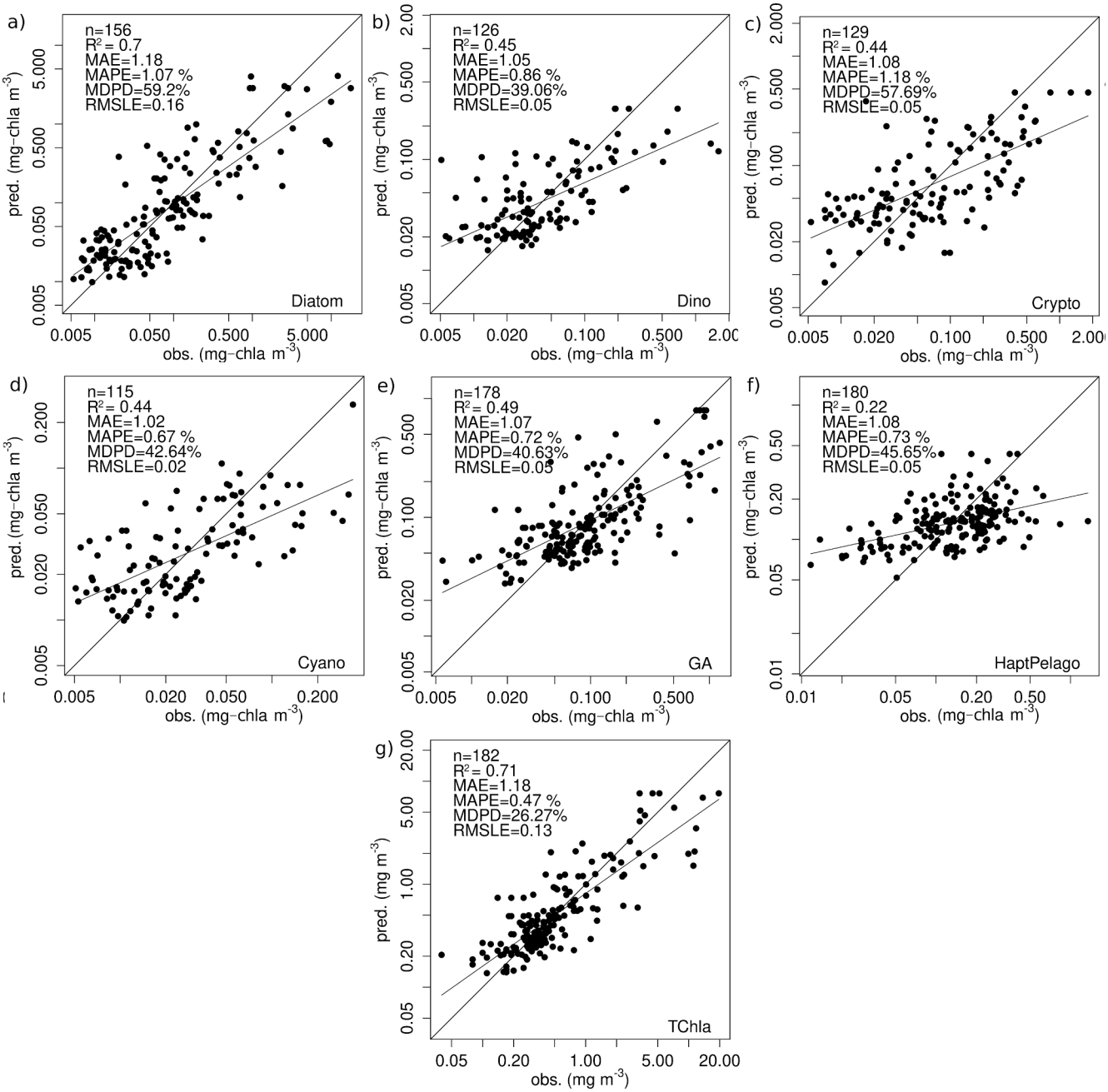

Fig. 6. Relationship between the predicted and *in situ* observed Chl-*a* [mg-chl m^{-3}] for each of the PFT (CHEMTAX-derived): a) diatoms, b) dinoflagellates, c) cryptophytes, d) cyanobacteria, e) green algae, f) haptophytes and pelagophytes, and h) total Chl-*a* [mg m^{-3}]. All scatterplots are presented in a log–log scale, and the MAE and R^2 were estimated based on the $\log_{10}$-transformed values.

significant high correlation coefficient between the *Synechococcus* spp. cell counts and CHEMTAX-dervived cyanobacteria Chl-*a* concentrations (mg-chl m^{-3}; r = 0.84, R^2 = 0.71, p < 0.001), demonstrating the overarching dominance of *Synechococcus* in the cyanobacteria group (Fig. 5a,c,d). A slightly lower but significant correlation was observed for similar comparisons for the cryptophytes group (r = 0.69; R^2 = 0.39, p < 0.001) (Fig. 5b). Moreover, the spatial distribution derived from the flow cytometry and pigment data showed that the hot spots of *Synechococcus* spp. cell counts (Fig. 5c) agreed in space with the CHEMTAX cyanobacteria abundance (Fig. 5d). Although cryptophytes showed more variability, the spatial pattern remained similar for both methods (Fig. 5e,f).

3.2.2. *Evaluation of the satellite-derived PFT*

Satellite-based PFT were derived for six phytoplankton groups, diatoms, dinoflagellates, cryptophytes, cyanobacteria, green algae, and the merged group consisting of haptophytes and pelagophytes (Fig. 6; Figure S5). Additionally, the HPLC-derived total Chl-*a* was added as a reference product to estimate the efficiency of the satellite data reconstruction of the Chl-*a* without the uncertainties introduced by the CHEMTAX analysis (Fig. 6g). The reconstruction quality was also increased by providing a relatively wide range of total Chl-*a* values, spanning from 0.08 up to 19.60 mg m^{-3}, even though the area of interest did not include the shelf areas (Fig. 1). The results show that, generally, the algorithms performed relatively well (p < 0.001), with R^2 remaining above 0.44, except for the hapto-pelago group (R^2 = 0.22, p < 0.001). Still, the MAE (1.08), the MAPE (0.73 %), and the MDPD (45.65 %) values were comparable to the other groups (Fig. 6f). The Chl-*a* diatom satellite retrieval resulted in a highly significant R^2 of 0.70 (p < 0.001), similar to the total Chl-*a* (R^2 = 0.71, p < 0.001) (Fig. 6a,g). For this group, the MAE and the RMSLE were also similar to the total Chl-*a*, with a MAE of 1.18 for both, and a RMSLE of 0.13 and 0.16, respectively. The diatom Chl-*a* reconstruction explained the highest proportion of the variance observed in the input data of all groups (R^2 = 0.70, Fig. 6a). Considering the other groups, the MAE and the RMSLE were the lowest for cyanobacteria, 1.02 and 0.02, respectively (Fig. 6d). The MAPE was the highest in cryptophytes (1.18 %) and the lowest for dinoflagellates (0.86 %) (Fig. 6b,c), which was also the group showing the lowest MDPD, 39.06 %. The measures derived using the cross-validation technique of 500 randomized runs on the subsampled data sets showed nearly as good results, with the MDPDcv, on average, 3 % higher than MDPD (Table S7). The RMSLEcv remained the same as the RMSLE for cyanobacteria, dinoflagellates, and the hapto-pelago group, and increased by 0.01 in all the remaining groups. The complete statistics can be found in the Supplement's Table S6.

3.3. *Identifying bioregions*

The bioregionalization was based on the input variables corresponding to the least correlated climatology-derived phenology metrics selected using Pearson's correlation coefficient results, as follows: start of the first bloom, start of the main (the most prolonged) bloom, end of

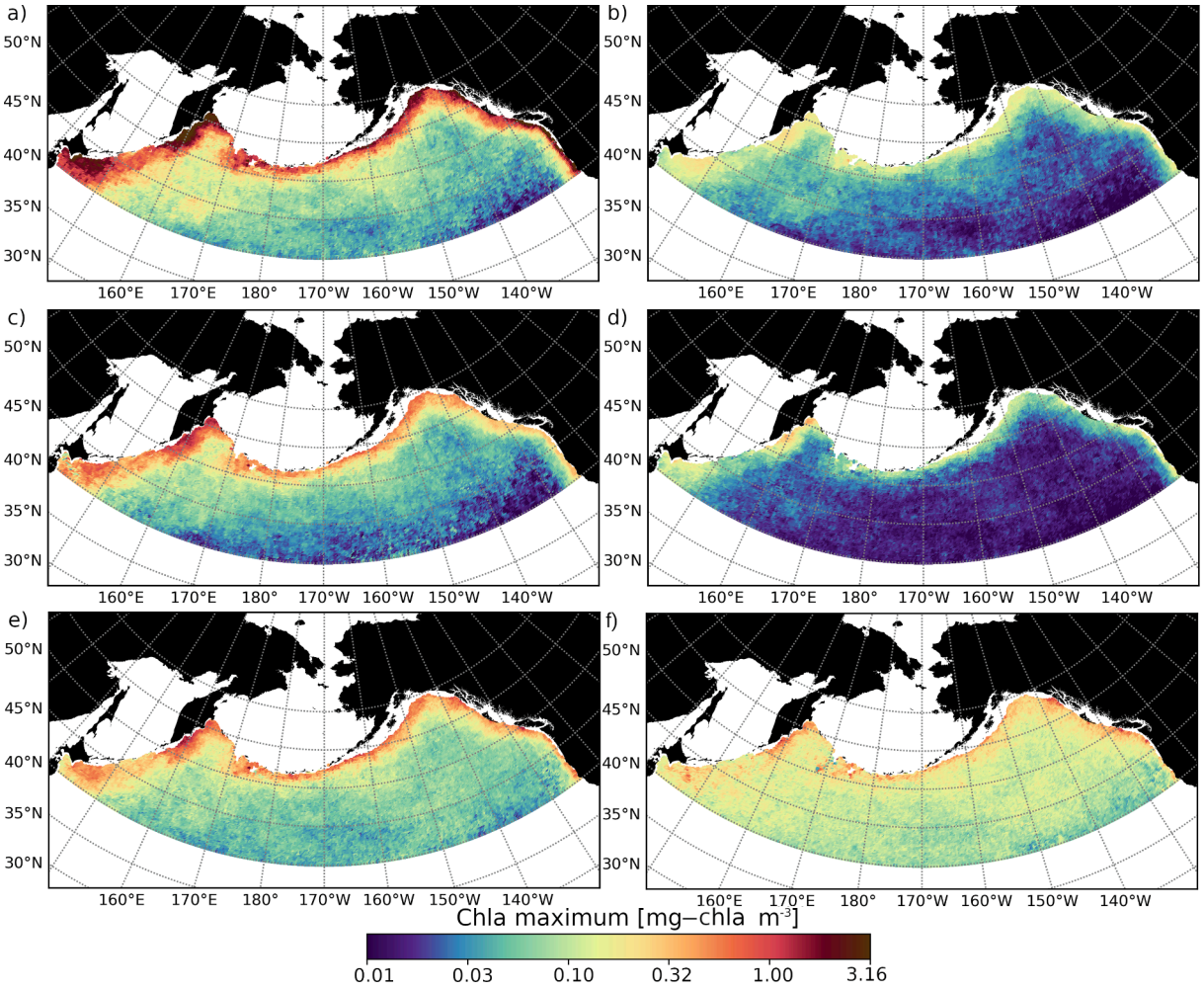

Fig. 7. Climatology (2002—2022) medians of the Chl-*a* maxima for each PFT: a) diatoms, b) dinoflagellates, c) cryptophytes, d) cyanobacteria, e) green algae, f) haptophytes and pelagophytes.

the last bloom, end of the main bloom, number of blooms, total bloom length, and Chl-*a* maximum value during the main bloom. That list of input variables was expanded by including the six satellite-derived PFT, thus allowing for variability related to changing proportions between the PFT to be included in the bioregionalization process (Fig. 7).

Each input variable was reflected in the SOM's structure (section 2.3), and their distribution across the nodes was presented in Figure S7. The analysis of the Silhouette index (Si) values revealed the main maximum at two classes (Si = 0.37; Figure S8), defining the primary separation between the central Pacific and areas near the continental slope (Fig. 8a), and the second local maximum at five classes (Si = 0.25; Figure S8), which was adopted as the final number of bioregions, named: Archipelago (Arch), Marginal (Mar), Connecting (Con), Central North (CN), and Central South (CS) (Fig. 8b; S9).

3.4. Characterization of the bioregions

The Central South (CS) bioregion had the lowest Chl-*a* concentrations and variability, with a particular decrease from July to September (between the 180th and 280th day of the year (DOY); Fig. 9a). In the Central North (CN) bioregion, Chl-*a* concentrations were nearly as low as in the CS, but with the lowest Chl-*a* in June, followed by an increase in late July to October (between the 200th and 300th DOY; Fig. 9b), responsible for the dominant fall-bloom pattern. The Connecting (Con), Marginal (Mar) and Archipelago (Arch) bioregions were located along the shelf break. In Con, two blooms of similar magnitude were apparent (Fig. 9c). Mar and Arch bioregions also showed a clear two-bloom cycle, but in Arch there was noticeable variability in the spring bloom Chl-*a* levels (Fig. 9e). Mar was the only bioregion with a prominent spring peak between April and early June (the 90th and 160th DOY) when generally the highest Chl-*a* maxima were recorded (Fig. 9d). In Mar, the secondary bloom observed in the fall was smaller than in spring, with similar Chl-*a* levels to the Arch fall bloom.

The timing of the first bloom and its character varied significantly across all the bioregions (Fig. 10a). The highest variability was observed in the central bioregions, CS and CN, where the spring bloom was negligible, and the first bloom and the main bloom started in late summer (Fig. 10c). In the Con and Mar bioregions, the onset of the first bloom occurred in late March and April and was much more pronounced than in the central CS and CN bioregions. The latest first bloom, started in June in the Arch bioregion (Fig. 10a). All regions showed significant differences in the timing of the main bloom start except between CN and Arch (Fig. 10b).

The length of the main bloom and the bloom season showed opposite tendencies (Fig. 10c,d). In CS, several Chl-*a* peaks of short duration were observed in the relatively long time span, suggesting small dynamic pulses of Chl-*a* rather than a clear bloom pattern (Fig. 9a). The total length of the blooms was the lowest in the CS and CN bioregions, and the difference between them was not statistically significant ($p > 0.05$) (Fig. 10e). In contrast, the total length of the blooms was the longest in Con and Mar, with the Mar bioregion also showing the highest Chl-*a* values, which were the primary feature distinguishing Mar in the SOM analysis (Fig. 10f). For the different bioregions, the Chl-*a* maxima showed a spatial trend where the lowest maxima were observed in open ocean waters, corresponding to CS and CN, followed by Con, Arch, and Mar, near the shelf break (Fig. 10f).

The relative contribution of each PFT varied significantly among the bioregions, reflecting the spatial distribution of the PFT Chl-*a* maxima (Fig. 9). The Mar bioregion, adjacent to the continental slope, was dominated by diatoms, contributing to almost half of the climatology median Chl-*a* maxima (48 %) (Fig. 9i). Diatoms were also a prominent group in Arch, constituting 38 % of the maximum Chl-*a* values, followed by cryptophytes (21 %), which were more abundant in this bioregion than in any other (Fig. 9j). In the Con bioregion, diatom contribution was 32 % (Fig. 9h), while the hapto-pelago group contribution was double that in the Mar bioregion. In the central Pacific CN, the hapto–pelago group was dominant, contributing to 31 % of the Chl-*a* maxima, followed by diatoms at 23 % (Fig. 9g). The lowest fraction of diatom Chl-*a* (17 %) was noted in the CS bioregion, where the hapto-pelago group dominated compared to the other groups, with a 37 % share (Fig. 9f). Cyanobacteria and green algae fractions were also more prominent in CS than in any other bioregion at 6 % and 21 %, respectively.

It is worth noting that diatoms overshadowed the other groups regarding the maximum Chl-*a* concentrations (Fig. 9). However, the seasonal proportions between the PFT Chl-a maximum values revealed the significant role of diatoms mainly between April and September, especially in the Mar bioregion (Fig. 11). In the other months, haptophytes and pelagophytes played a dominant role, and in CS and CN, the hapto-pelago group dominated all year. Green algae and the hapto-pelago group constituted 50 % – 70 % of total Chl-*a* (Fig. 11).

4. Discussion

This study presents a novel division of the subarctic Pacific Ocean into five bioregions based on phytoplankton phenology metrics and functional groups obtained from 20+ years of GlobColour satellite products. The bioregions reflect spatial differences in phytoplankton dynamics and community composition, generally dominated by green algae, haptophytes and pelagophytes (Fig. 11), and a gradually increasing diatom share towards the North Pacific basin continental margins. Challenges associated with data preparation are discussed below, starting with the influence of missing values, the interpolation method, the adopted baseline, and the definition of a bloom from the phytoplankton phenology metrics (section 4.1). Then, the general retrieval quality of the distribution of PFT in the subarctic Pacific, the CHEMTAX analysis results, and the number of retrieved PFT are compared with previous research (section 4.2). Finally, each identified bioregion is considered in the broader context of previous published dynamics and divisions of the subarctic Pacific, including possible ecosystem implications (section 4.3).

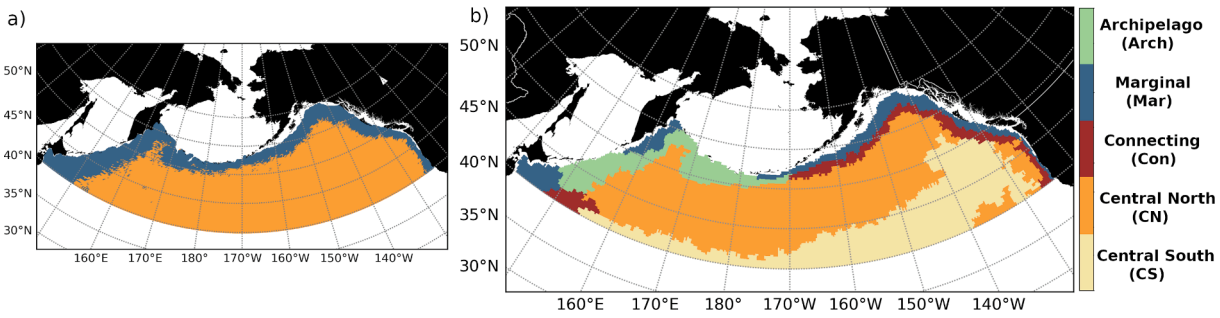

Fig. 8. (a) The primary division of the subarctic Pacific into the central basin and the continental slope area, and (b) the final five bioregions: Archipelago (Arch), Marginal (Mar), Connecting (Con), Central North (CN) and Central South (CS).

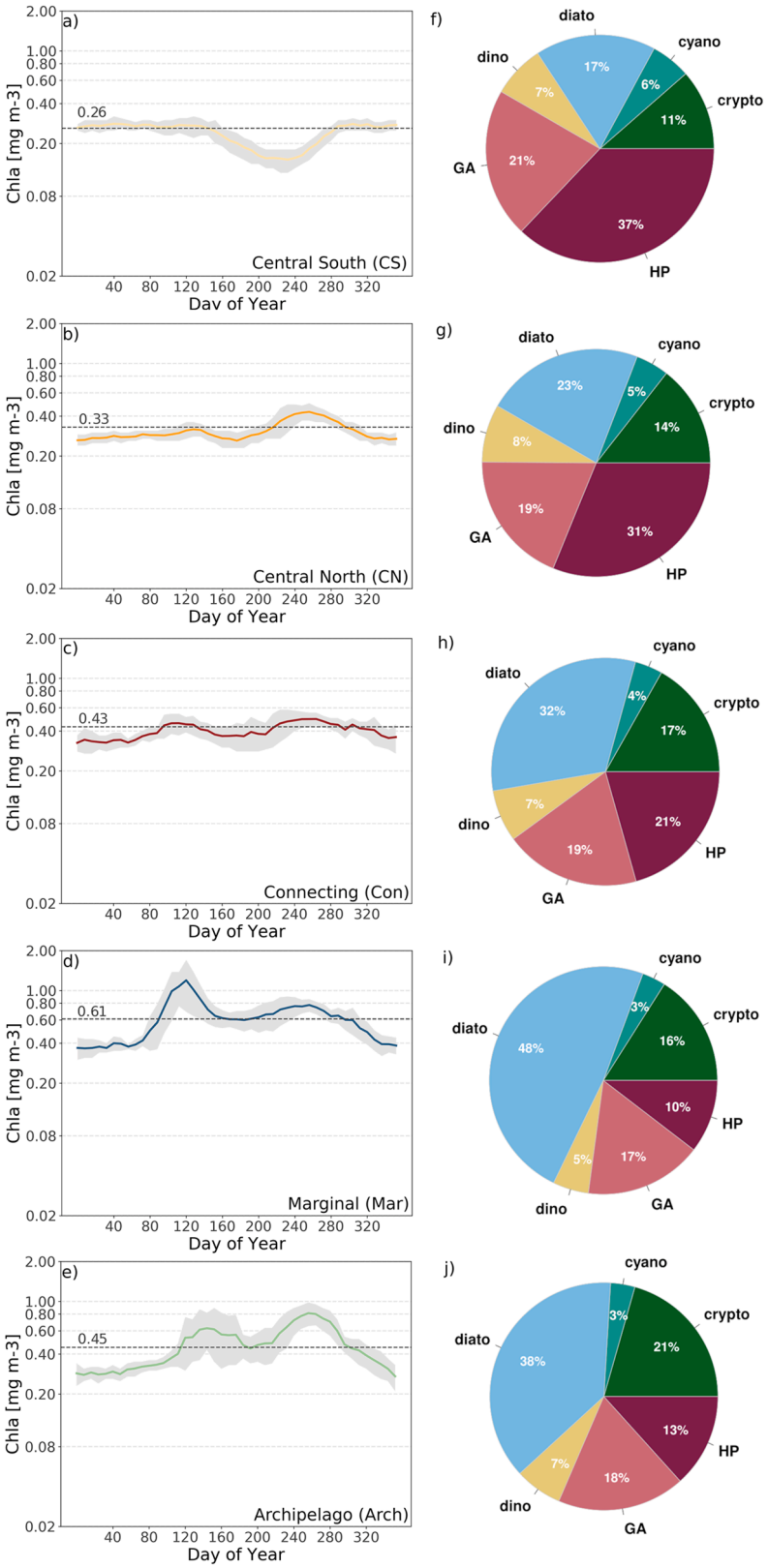

Fig. 9. Left panel: the climatological seasonal cycles of Chl-*a* [mg m^{-3}] at each bioregion: a) Central South (CS), b) Central North (CN), c) Connecting (Con), d) Marginal (Mar), e) Archipelago (Arch). The shaded areas represent (±σ), and the lines' colours correspond with the bioregions in Fig. 8; the dark dotted lines represent the baseline used to derive phenology metrics. Right panel: phytoplankton communities composition based on the yearly PFT Chl-a maxima within each bioregion f) Central South (CS), g) Central North (CN), h) Connecting (Con), i) Marginal (Mar), j) Archipelago (Arch). The following abbreviations were used: 'cyano' – cyanobacteria, 'crypto' – cryptophytes, 'diato' – diatoms, 'dino' – dinoflagellates, 'GA' – green algae, 'HP' – haptophytes + pelagophytes.

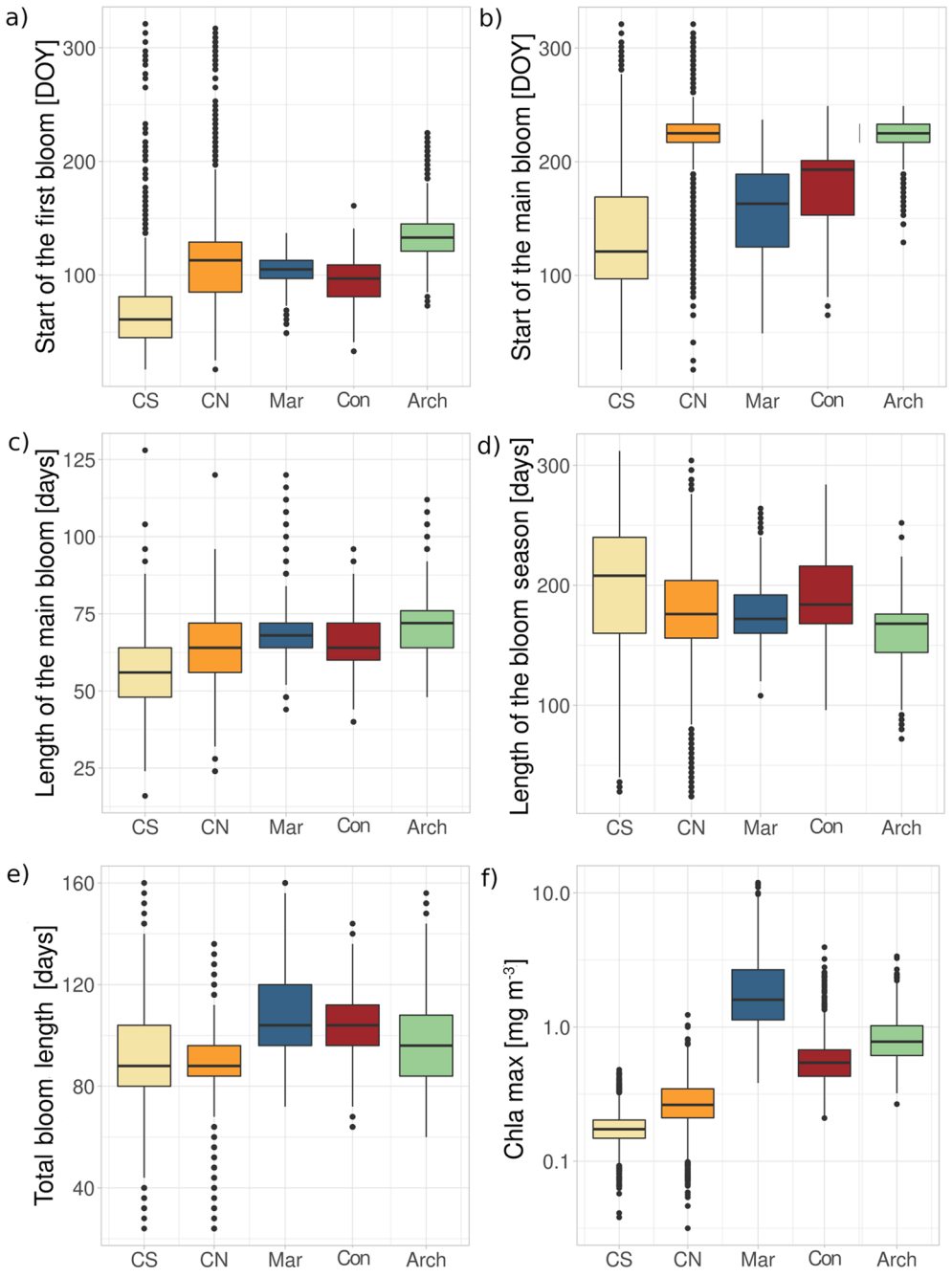

Fig. 10. Boxplots presenting variability of: a) start of the first bloom [Day Of Year], b) start of the main (the most prolonged) bloom [Day Of Year], c) length of the main bloom [days], d) length of the bloom season (time between the start of the first bloom and the end of the last one) [days], e) total bloom length [days], f) Chl-*a* maximum [mg m^{-3}], within each of the five bioregions. The boxplots' colours correspond with the bioregions in Fig. 8. The centre line represents the median value, the box stretches between 25% and 75% quantile, whiskers span an additional 1.5IQR up and down, and the dots represent the outliers.

4.1. Defining phytoplankton phenology

The phytoplankton phenology metrics were determined using the Chl-*a* threshold method due to its effectiveness for match/mismatch analysis with higher trophic levels and less sensitivity to the timeline start date (Brody et al., 2013). However, to correctly interpret the phytoplankton phenology results and their impact on the final bio-regionalization, we must consider the methods used to define the phenology metrics and the input data pre-processing. The effect of clouds must be regarded as they may obscure critical features related to the bloom start date in early spring, or result in a significant rise of the yearly average Chl-*a* due to missing wintertime data (Brody et al., 2013). Thus, the chosen time range and yearly division indirectly affect the Chl-*a* baseline level. To minimize these effects, and given the varying amounts of missing spatial data in different years, our analysis adopted the Chl-*a* climatology baseline to define phytoplankton phenology metrics, which was generally less affected by seasonal data availability. Further, a year was defined from January to December, and missing values at the ends were not interpolated since interpolation of large or systematic gaps may introduce unnecessary uncertainty (Buttlar et al., 2014). Additionally, light limitation of primary productivity was assumed for the study area stretching north of the 40°N parallel. Previously reported end-of-year increases of Chl-*a* (Wilson and Coles, 2005; Yoo et al., 2008) were related instead to phytoplankton

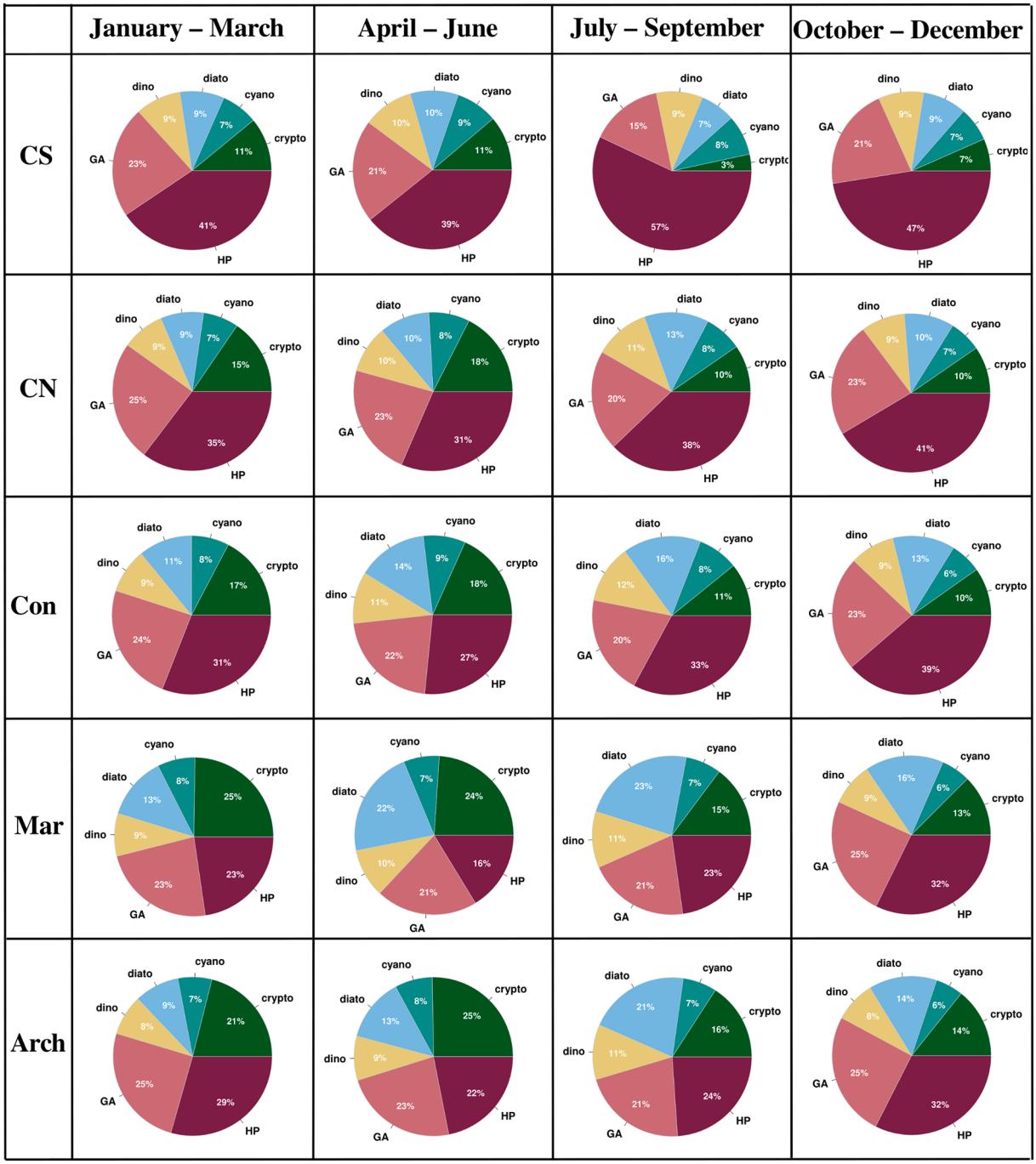

Fig. 11. Seasonal composition of the phytoplankton communities within bioregions based on climatology medians. The following abbreviations were used: 'cyano' – cyanobacteria, 'crypto' – cryptophytes, 'diato' – diatoms, 'dino' – dinoflagellates, 'GA' – green algae, 'HP' – haptophytes + pelagophytes.

photoacclimation or intense vertical mixing that brought phytoplankton from the deep Chl-*a* maximum to the surface, resembling blooms observed with remote sensing data.

From an ecological point of view, a bloom is an event of rapid phytoplankton growth dominated by a single taxon (Isles and Pomati, 2021). By this definition, blooms were evident near the continental slope, where pronounced peaks in Chl-*a* were observed (>1.0 mg m^{-3}), and diatoms dominated the community composition (Figs. 9, 11). By contrast, in the middle of the Alaskan Gyre, seasonal variability was minor, with the yearly coefficients of variance below the threshold (0.35) proposed by Cole et al. (2012). However, we found that relatively small Chl-*a* concentrations and low variability were distinct climatology traits essential for bioregionalization (Figure S7). This study used the term bloom for any Chl-*a* increase above the climatology baseline that lasted longer than two weeks (Soppa et al., 2016; Krug et al., 2018; Suchy et al., 2022). Such a broad definition was flexible enough to fully describe phytoplankton dynamics and detect a wide variety of Chl-*a* changes, including typical single blooms possible to describe using a Gaussian curve, overlapping blooms of a bimodal shape, and flattened persistent Chl-*a* increases (Isles and Pomati, 2021). It is worth noting that Chl-*a* dynamics may also result from the vertical and horizontal transport of existing biomass rather than biological growth processes (Isles and Pomati, 2021), called "advective blooms." Those were described by Isles and Pomati (2021) as algal biomass increase, often identified as a bloom by phenology metrics, resulting from an intrusion of water masses of varying properties. Such a change in Chl-*a* of external

origin may have been observed in the three-bloom areas, which co-occurred with the TZCF (Fig. 4b).

To confirm the reliability of our results, the obtained phenology metrics were compared with values in the literature, with particular attention paid to the timing of bloom initiation. In the area close to Japan (Mar and Arch), the beginning of the first bloom ranged between the 73rd and 83rd DOY, corresponding to the second half of March. The first bloom lasted around 90 days (Fig. 4a), with maximum Chl-*a* in the middle of April, between the 105th and 113th DOY, and bloom ending time around 161st and 177th DOY, corresponding to the second half of June. This phenology pattern is similar to a 10-year Chl-*a* cycle determined by Okamoto et al. (2010) for this region. A similar pattern, with a well-defined spring bloom, was also identified around Alaska (Mar). The start of the bloom in this region was estimated at the beginning of April and May (between the 105th and 133rd DOY; Fig. 4a), and the Chl-*a* peaked in May, which is consistent with the findings by Waite and Mueter (2013). Here and in Waite and Mueter (2013), a second Chl-*a* increase was also observed in the second part of August and in September (here appearing between the 230th and 260th DOY; Fig. 4c). Close to British Columbia, bloom timing followed patterns recently described by Marchese et al. (2022), with a noticeably earlier spring bloom onset in the southern section in March (between 60th and 80th DOY), at the beginning of April (90th DOY) closer to the shore, and in the second half of April (between the 100th and 120th DOY) in the north of BC (Fig. 4a). Moreover, the fall bloom was dominant in this area (Fig. 4c). For waters east of the Kamchatka Peninsula, the spring bloom occurred in late April (between the 100th and 120th DOY) and between May and early June (between the 120th and 170th DOY) around the Kuril Islands, as previously reported by Racault et al. (2012). Similar to the study by Yoo et al. (2008), the main bloom in the open waters of the Pacific was generally detected in the second half of the year, except for the Kamchatka Peninsula region, where the beginning of the main bloom was observed at the turn of August and September, and lasting until the first part of November (between the 220th and 320th DOY; Fig. 4c).

The region southwest of the Aleutian Archipelago had the latest bloom start, about two months later than in the Alaska area (Fig. 4a), even though the waters in the Aleutian Archipelago are regularly supplied with iron by water exchange with the Bering Sea (Nishioka et al., 2021), and the average light levels are comparable to the Alaskan coast due to similar latitudinal location (Fig. 4). Delayed water column stratification is considered the primary factor controlling phytoplankton growth in this region (Goes et al., 2004). Considering these factors, the late first bloom observed for the Aleutian Archipelago is likely associated with a delay in mixed layer shoaling to the critical depth described by Sverdrup's theory (Smetacek and Passow, 1990). In this region, Abe and Nakamura (2013) described turbulent mixing mechanisms related to tidal water flow, causing formation and breaking of Lee waves due to the topography around the Aleutian Archipelago, and diapycnal mixing, leading to deepening of the mixed layer and weak water column stratification. The deep mixed layer depth around the central and western Aleutian passages has also been documented by Suga et al. (2004).

The deep mixing south of the central and western Aleutian Islands may provide a mechanism of iron enrichment in this area, potentially stimulating phytoplankton growth. To investigate the possible spatial overlap between the diapycnal mixing areas and increased phytoplankton abundance, we roughly estimated the spatial distribution of the total bloom magnitude, defined as the yearly accumulated Chl-*a* [mg m^{-3} year^{-1}] during the bloom period (Fig. 12), as a proxy. The higher Chl-*a* maxima noticeably increased bloom magnitudes around the continental slope (Fig. 4h, 12), especially along the Kuril Islands where diapycnal mixing was significant. However, the total bloom magnitude was shaped mainly by the total length of the blooms, limited by sunlight in the northern regions. South of the central and western Aleutian Islands (Fig. 12), however, the weaker stratification of the water column (mentioned above) suppressed phytoplankton growth despite the likely higher iron supply in this region. Nevertheless, the smallest bloom magnitude was observed in the south, along the NPTZ, and the central subarctic Pacific (Fig. 12), where weak advection and mixing (Ayers and Lozier, 2010; Ueno et al., 2023) and dust deposition are the main sources of the iron that stimulate productivity (Fiechter et al., 2009).

Although clear spatial patterns of bloom magnitude were observed in this study, particular caution must be applied while drawing conclusions on phytoplankton productivity in the area since the carbon to Chl-*a* ratio varies across the subarctic Pacific (Burt et al., 2018), and Chl-*a* variability does not fully represent changes in biomass (Britten et al., 2022). Furthermore, zooplankton grazing is known to significantly impact phytoplankton abundance and community structure in the area (Strom and Welschmeyer, 1991; Tsuda et al., 2007), likely suppressing Chl-*a* concentrations. Previous research (e.g., Goes et al., 2004) suggested that the permanently shallow-residing pycnocline in the eastern part of the subarctic Pacific sustains comparable levels of small-algae growth all year long and supports micrograzers survival over winter. In spring, grazers consume the excess algae production, and weak vertical mixing limits silicate and iron renewal, preventing diatoms from forming intense spring blooms. A change around September, in both algae and zooplankton compositions, overlaps with the short-term advantage of algae growth over grazing, which is likely visible as fall blooms (Yoo et al., 2008). However, the coupling between the phyto- and zooplankton is tight and complex (Strom and Welschmeyer, 1991), so the conclusions must be drawn carefully.

4.2. Phytoplankton groups

Validation of the CHEMTAX's results against the independent *in situ* flow cytometry dataset (Peperzak et al., 2018; Eisner and Lomas, 2022) showed high correlation between the CHEMTAX-derived groups (in mg-chl m^{-3}) and the flow cytometry measurements (in cells ml^{-1}), and the spatial distributions of data from both sources matched well (Fig. 5). This validation allowed us only to compare two phytoplankton groups out of six. However, since CHEMTAX derives the quantitative contribution of phytoplankton groups to the total Chl-*a* concentration, groups are highly intertwined (Mackey et al., 1996), and good agreement for the two tested groups significantly increases the reliability of the resulting estimation for all groups. Similarly, in many other studies, only selected groups were validated, depending on the *in situ* data availability (Del Bel Belluz et al., 2021; Fujiki et al., 2009; Isada et al., 2019; Pan et al., 2011).

The PFT selection for the satellite algorithm development was based on the specificity of the subarctic Pacific waters and, considering the spectral constraints, where 9 R_{rs} GlobColour bands allowed for distinguishing six phytoplankton groups, comparable to the previous satellite-based PFT research by Alvain et al. (2005) and Xi et al. (2020), who computed 4 PFT (using 5 R_{rs} bands) and 6 PFT (using 10–12 R_{rs} bands), respectively. The spatial distribution obtained for the major

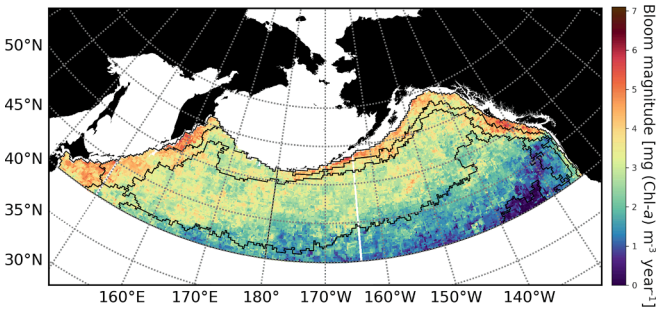

Fig. 12. The total magnitude of the blooms computed as the yearly accumulated Chl-*a* [mg m^{-3} year^{-1}] during the bloom period, with black lines outlining bioregions.

groups was consistent with the general characteristics of this area (Obayashi et al., 2001; Suzuki et al., 2002b; Fujiki et al., 2014; Isada et al., 2009; Peña et al., 2019; Wang et al., 2022; Waga et al., 2022). Generally, the influence of nutrient availability was reflected in the structure of phytoplankton assemblages (Fig. 11), with an increase of diatoms towards the continental, which are regions under naturally higher macronutrients and iron supplies (Strom et al., 2006; Nishioka et al., 2021), accompanied by dinoflagellates (Wang et al., 2022) and cryptophytes (Waga et al., 2022). The results showed an overlap in the spatial distribution of these three groups (Fig. 7a–c), but diatoms dominated the Chl-*a* maxima, indicating that this phytoplankton group is a major part of the biogeochemical carbon cycle and dominates export production (Sarthou et al., 2005; Brzezinski et al., 2022).

Apart from diatoms, the green algae and hapto-pelago groups were confirmed to be the main secondary contributors to Chl-*a* max, similar to the results by Obayashi et al. (2001). The Chl-*a* related to green algae, haptophytes and pelagophytes showed less seasonal variability (Fig. 11), and in the subarctic Pacific has been described as the 'basic structure' of the phytoplankton community (Obayashi et al., 2001; Suzuki et al., 2002b). In the open ocean, these groups dominated all year round, but closer to the shelf break, spring and summer blooms of diatoms were observed, described in previous studies as 'extra diatoms input' (Suzuki et al., 2002b; Alvain et al., 2005). We showed that rapid diatom growth markedly changed group proportions (Fig. 11), and we also observed an increase in cryptophytes biomass in April and May east of the Kuril Islands (Fig. 11), which has been described in the literature (Obayashi et al., 2001; Isada et al., 2019).

4.3. Overview of the bioregionalization

The bioregionalization obtained in this study for the subarctic Pacific revealed differences in phytoplankton composition and phenology patterns between the central Pacific waters and its margins. Two basin bioregions were identified, CS and CN (Fig. 8b), dominated by the hapto-pelago group and green algae, with low Chl-*a* and a highly variable Chl-*a* seasonal cycle. Towards the basin continental margins, the bioregion shifted to Con, and then the Arch and Mar bioregions, where the spring diatom bloom was evident, and the Chl-*a* maxima were the highest. In a recent classification presented by Sonnewald et al. (2020), where a 3D ecosystem model encompassing 35 phytoplankton and 16 zooplankton types was used, the subarctic Pacific was considered one province. Responsible for that may be the iron limitation impact varying with the observation scale. On the one hand, globally, iron limitation results in a distinct phytoplankton structure in the subarctic Pacific since it is one of only three HNLC zones in the entire World Ocean (Nishioka et al., 2021). On the other hand, in situ phytoplankton measurements (Suzuki et al., 2002a; Fujiki et al., 2009) and previous phytoplankton phenology analyses in the subarctic Pacific showed significant east–west differences, for example, between the Oyashio and the Alaska regions (Yoo et al., 2008; Sasaoka et al., 2011), which was the primary motivation for this bioregionalization. We limited our study area to the subarctic Pacific to investigate the variability within this region (Fig. 13b). The spatial distribution of the revealed bioregions was generally similar to the satellite-based Chl-*a* partitioning of the epipelagic zone by Longhurst et al. (1995), outlining the main hydrological patterns, such as the Alaska Downwelling Coastal Province, the California Upwelling Coastal Province, the Kuroshio Current, the Pacific Subarctic Gyre East and West, and the North Pacific Polar Front (Fig. 13a). However, some differences were noted, which may stem from the fact that the study by Longhurst et al. (1995) was based on the 1° spatial resolution data obtained from the Coastal Zone Color Scanner (CZCS), much coarser than the 25 km spatial resolution used in this study, and on a shorter time series. Moreover, their input was a total Chl-*a* data series, whereas, in this study, we investigated the phytoplankton phenology and incorporated information about the PFT distribution.

Beyond comparing with the previous partitioning, it is essential to compare our results with the spatial variability in the physical and biogeochemical water properties. In recent research, Ueno et al. (2023) presented relationships between the Sea Surface Height (SSH) anomaly, eddy kinetic energy, and Chl-*a*, which underlined the importance of mesoscale eddy formation for nutrient transport in the entire ecosystem. The correspondence in space between Ueno et al.'s areas of enhanced mixing and physical transport offshore, and the higher bloom magnitude in our study, suggests a significant impact of the iron supply mechanisms on the phytoplankton phenology and composition (Obayashi et al., 2001; Strom et al., 2006; Nishioka et al., 2021), in addition to light limitation. This was particularly evident in the Mar bioregion because of the large share of diatoms, known for their sensitivity to iron shortages (Sarthou et al., 2005). Furthermore, retrieved bioregions resembled the spatial distribution of the dissolved iron-to-nitrogen ratio (dFe/N) in the upper-intermediate waters presented by Nishioka et al. (2020). This relationship between our bioregions and iron distribution may be one of the key findings worth further analysis. Each bioregion showed distinct features, which are summarized in Table 2 and discussed below.

4.3.1. Central South bioregion

The central south (CS) bioregion overlapped with the North Pacific Polar Front province outlined by Longhurst et al. (1995) where the subtropical and the subarctic Pacific gyres converge, parallel to the TZCF, located south of the 40°N for most of the year (Ayers and Lozier, 2010; Polovina et al., 2001). In summer, however, the TZCF shifts beyond 40°N and reaches the northernmost position around August. That seasonal shift of the TZCF covered the CS bioregion when the Chl-*a* values dropped between July and September (Fig. 14), agreeing with the TZCF position described by Polovina et al. (2001). Chl-*a* maxima in CS were generally the lowest (~0.3 mg m^{-3}), and the observed patterns may have been caused by the influence of the lower Chl-*a* transition waters, making the Chl-*a* concentrations in February–March and November appear as bloom conditions (Fig. 9a, 14). Thus, the impact of the TZCF zone on the phenology metrics in CS should be considered when interpreting the results in a broader context. Additionally, the TZCF influence was confirmed by the contrast between spring and summer phytoplankton communities, with the more pronounced presence of cryptophytes and green algae in winter and spring that rapidly turned into the dominance of haptophytes and pelagophytes in summer months (Fig. 11). The occasional *Prochlorococcus* appearance indicated a possible intrusion of subtropical waters (Suzuki et al., 2005). The TZCF presence is generally associated with a decrease in primary productivity in this bioregion (Fig. 14), but it should also be viewed as a critical area for higher trophic levels since it is related to the North Pacific Current, considered a major migration route for many marine species (Polovina et al., 2001; Polovina et al., 2017), including nekton predators, such as albacore, flying squid, loggerhead turtles, and blue sharks (Pearcy, 1991; Polovina et al., 2001).

4.3.2. Central North bioregion

The central north (CN) bioregion covers relatively homogeneous waters of the HNLC region of the subarctic Pacific, including the Alaskan Gyre and central subarctic Pacific (Fig. 8b), where iron limitation (Nishioka et al., 2021) and zooplankton grazing (Strom and Welschmeyer, 1991; Fujiki et al., 2009) are important factors determining phytoplankton biomass. This region was characterized by low seasonal variations, fall blooms of relatively short duration, and the second lowest Chl-*a* maxima (Fig. 10f), where green algae, haptophytes and pelagophtyes dominated throughout the year (Fig. 11). Chl-*a* concentrations and phytoplankton community structure were comparable to the CS bioregion, with more cryptophytes in spring and fewer haptophytes and pelagophytes in summer, thus suggesting that the primary difference between the two was related to the influence of the TZCF in the CS.

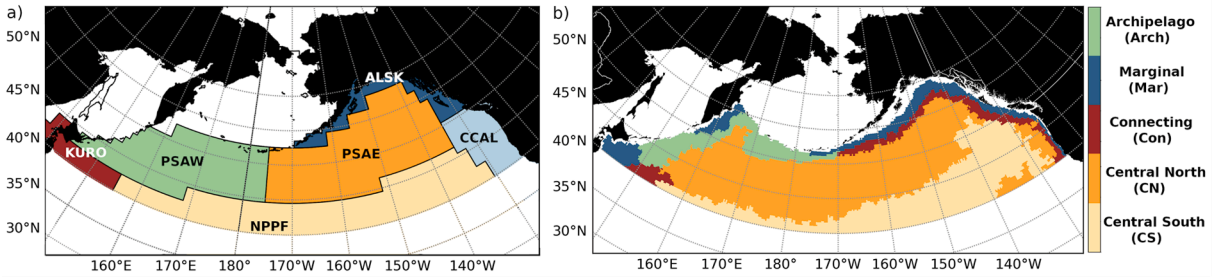

Fig. 13. Comparison of: a) provinces delineated by Longhurst et al. (1995), where KURO – Kuroshio Current Province, NPPF – N. Pacific Polar Front Province, PSAW – Pacific Subarctic Gyre (West), PSAE – Pacific Subarctic Gyre (East), ALSK – Alaska Downwelling Coastal Province, CCAL – California Upwelling Coastal Province, and b) bioregions defined in this study.

Table 2
A summary of the bioregion main characteristics.

Type	Name	Characteristic features	
Central	*Central South (CS)*		The southernmost bioregion influenced by the NPTZ, with the lowest Chl-*a*, the lack of typical bloom pattern, and the largest share of haptophytes and pelagophytes of all bioregions.
Central	*Central North (CN)*		The central subarctic Pacific bioregion, with the second lowest Chl-*a* and the second largest share of haptophytes and pelagophytes after CS, the total bloom time below 100 days, and a clear fall-bloom pattern, where the main bloom starts after the 200th DOY.
Continental Slope	*Connecting (Con)*		The connecting bioregion with two similar blooms, Chl-*a* generally < 0.6 mg m^{-3}, and the main bloom starting on average later than in the Mar bioregion, but earlier compared to CN and Arch.
Continental Slope	*Marginal (Mar)*		The marginal bioregion, the closest to the continental slope, with the highest Chl-*a* and the largest diatoms share of all bioregions, a prominent spring bloom (reaching on average 2 mg m^{-3}), and the longest total bloom time (up to ~ 120 days).
Continental Slope	*Archipelago (Arch)*		The island-bordered bioregion, located along the Kuril and the Aleutian Archipelagos, with significant presence of diatoms, the second highest Chl-*a* and the latest start of the first bloom (> 100th DOY), with the fall (200th DOY) blooms predominance.

4.3.3. *Connecting bioregion*

The connecting (Con) was the smallest bioregion identified, and located between the low-Chl-*a* CN and the highly-productive, coastal-influenced Mar bioregion. The phytoplankton communities in the Con were dominated by haptophytes and pelagophytes in fall and winter, similar to CN, yet with a significant presence of diatoms and dinoflagellates in spring and summer, similar to Mar (Fig. 11). The spring and summer blooms were nearly even in magnitude (Fig. 9c). Geographically, in the east, Con was located at the boundary of the Alaskan Gyre, within the reach of mesoscale eddies originating off the shelf, but under smaller nutrient supplies than Mar, which resulted in Chl-*a* variability patterns distinct from the adjacent Mar and CN bioregions. In the west, Con also overlapped with the area of mesoscale mixing due to the Kuroshio and the Oyashio currents interaction, where the Kuroshio Bifurcation zone forms (Isoguchi et al., 2006). The Oyashio current introduces cool subarctic water masses of lower salinity but significantly higher nutrient loads than the subtropical Kuroshio waters, which are warmer, more saline, and oligotrophic (Yatsu et al., 2013). In this region, intrusions of the Kuroshio Extension jets are responsible for the observed lower Chl-*a* concentrations, comparable to the Con bioregion characteristics in the east, despite the differences in temperature and salinity between the eastern and western parts of Con. This region is also recognized as a crucial feeding area for small fish like Japanese sardines or chub mackerel that migrate with the waters propagating northward, providing sufficient food to juveniles to sustain their growth and recruitment (Isoguchi et al., 2006; Shiozaki et al., 2014). The abundance of food may be related to the relatively long total bloom duration observed in the Con (Fig. 4f) and moderate Chl-*a* concentrations (Fig. 4h).

4.3.4. *Marginal bioregion*

The highest bloom magnitude among the bioregions was noted in the Marginal (Mar) bioregion (Fig. 12), stretching along the continental slope, except for the areas adjacent to the Kuril Islands and the Aleutian Islands (Fig. 8b). The most striking features of Mar were the significantly higher Chl-*a* maxima, prominent spring bloom peak with Chl-*a* values exceeding 1.0 mg m^{-3} (Fig. 9d), and evident 'extra diatoms input' to the total Chl-*a* maxima indicated in the phytoplankton composition (Fig. 11). Mar overlapped with waters intensely enriched in iron from external sources (Nishioka et al., 2021), which on the British Columbia

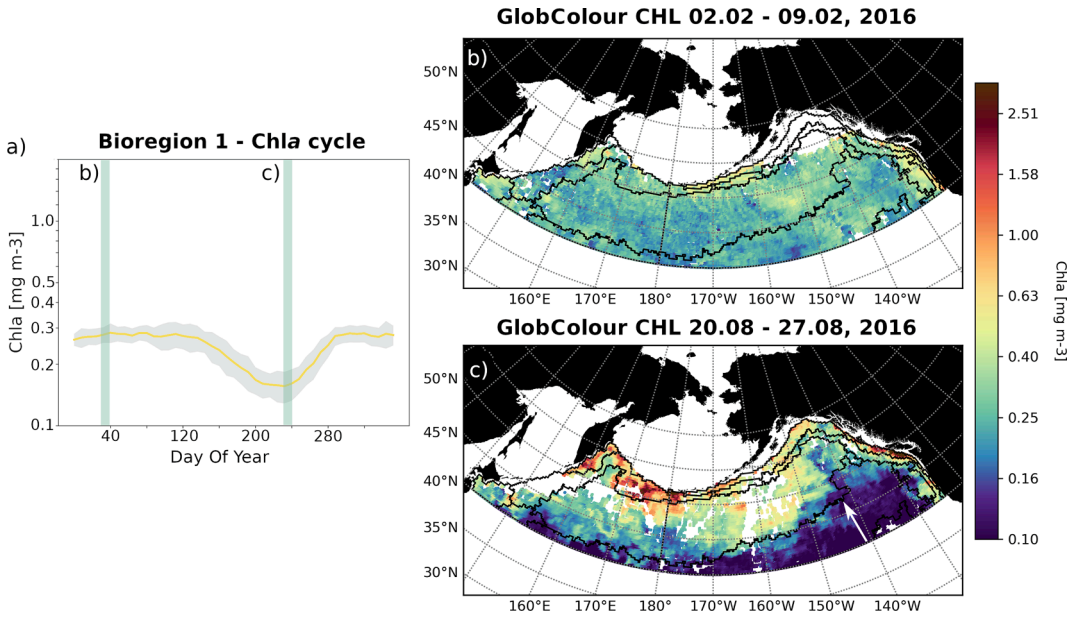

Fig. 14. The a) annual cycle of Chl-*a* [mg m^{-3}] in the Central South (CS) bioregion, where the green vertical lines mark the two extreme positions of the Transition Zone Chlorophyll Front (TZCF). Maps of the satellite-derived Chl-*a* concentration b) on February 2^{nd} – 9^{th}, 2016, presents the average Chl-*a* levels, and are contrasted with the maximum area of the TZCF, with the Chl-*a* below 0.2 mg m^{-3}, c) on August 20^{th} – 27^{th}, 2016, which shifts northwards in summer as depicted by the white arrow. Both maps were overlaid with the bioregions outline to show the spatial overlap between the TZCF-influenced area and the CS bioregion.

and Alaska coasts is derived from river discharge, glacial meltwater, shelf sediment resuspension, and dust deposition (Whitney et al., 2005; Cullen et al., 2009; Davis et al., 2014; Crusius et al., 2017; Crusius, 2021). In the western Pacific, the input of Okhotsk Seawater (Sugie et al., 2010) and freshwater runoff from the Kamchatka Peninsula (Nishioka et al., 2021) contributed to higher productivity. In addition, mesoscale eddies that form on the Pacific shelf transport nutrients offshore, especially the Haida eddy (Whitney et al., 2005), the Sitka, and the Yakutat eddies. Those three, have been considered the most impactful on the biogeochemical cycles of the Alaska region (Rovegno et al., 2009), influencing also the Con, and possibly the CN bioregions. The differentiation of Mar proved the enormous impact of mesoscale transport of coastal nutrients on phytoplankton productivity and community structure. Those findings are particularly interesting when combined with the research by Healey et al. (2000) on the lower metabolic costs for salmon stocks migrating back to the spawning grounds crossing the eddies in the Gulf of Alaska.

4.3.5. *Archipelago bioregion*

The Archipelago (Arch) bioregion represents the areas adjacent to the Okhotsk Sea and the western Bering Sea (Fig. 8b), which are essential sources of iron for the western subarctic Pacific (Nishioka et al., 2021). In those regions, strong tidal flows transporting water across the Kuril and Aleutian Archipelagos trigger intense vertical mixing (Nakamura et al., 2000; Abe and Nakamura, 2013) and enforce nutrient enrichment. The most pronounced water exchange with the Bering Sea is observed west of Amchitka Pass (Abe and Nakamura, 2013), which overlaps with the easternmost part of the Arch bioregion (Hunt and Stabeno, 2005). Mixing across the Aleutian passages also affects the timing of water column stratification (Goes et al., 2004; Suga et al., 2004; Abe and Nakamura, 2013), possibly explaining the late blooms, single-bloom patterns, and short yet intense bloom seasons shown by phenology metrics (Fig. 4b,c,g). Slightly lower observed bloom magnitude (Fig. 12) and Chl-*a* maxima (Fig. 10f) may have been caused by intense zooplankton grazing (Fujiki et al., 2009), suggested as being a significant factor suppressing primary production (Strom and Welschmeyer, 1991; Naidenko, 2001; Tsuda et al., 2007), yet impossible to estimate from the satellites. In comparison, the positive impact of the more nutrient-rich Okhotsk Intermediate Water on the primary production of this region has been documented in the literature (Nakamura et al., 2000; Yasuda et al., 2002), and was evident in the extreme length of the main bloom, the total bloom length, and the Chl-*a* maxima in this bioregion (Fig. 4e,f,h). Interestingly, the research by Waga et al. (2022) also showed an increased share of cryptophytes in the phytoplankton communities, especially at the post-bloom stage, similar to our findings for this region (Fig. 11). Apart from having the highest share of cryptophytes, the phytoplankton community structure was comparable to the Mar bioregion, except for the lower diatom contribution (Fig. 11).

5. Data and method limitations

The restriction of the available satellite images in time should be considered while interpreting our study results. The 8-day binning period was optimal for minimizing missing data due to cloud cover and the precision of the phytoplankton phenology determination, which has been a common choice across the literature (Yoo et al., 2008; Marchese et al., 2017; Krug et al., 2018; Lavigne et al., 2018; Suchy et al., 2022). The other aspect to consider is the development of reflectance-based algorithms dedicated to phytoplankton functional types, partially constrained by the available R_{rs} bands, cloud-free pixels, and the number of in situ HPLC samples. These factors reduced more than one thousand measurements to almost 200 matchups. Although not a large data set, it is comparable to those used in previous studies (Moisan et al., 2017; Xi et al., 2020; Vishnu et al., 2022). There is also, in general, very little *in situ* data to verify the satellite PFT output, which needs to be addressed in the near future (Bracher et al., 2017).

Another source of uncertainty is related to the in situ PFT estimation associated with the HPLC method and the CHEMTAX analysis assumptions of no photoadaptation or photoacclimation processes, which is a considerable oversimplification given the broad latitudinal range considered. Diurnal cycles, downwelling irradiance, spectral characteristics of available light, nutrient concentrations, and growth phase, among many others, severely impact the temporary pigment composition and may cause variability between populations of the same species (Higgins et al., 2011). To minimize these effects, in this research, the phytoplankton composition was determined based on subsets (clusters;

Figure S4) of samples with similar pigment proportions collected in the surface layer, and the results were validated against flow cytometry samples. Nonetheless, some specific phytoplankton groups, like calcifiers (e.g., coccolithophorids), whose absorption spectra are related to their outer scales presence rather than their Chl-*a* content or mixotrophs that may have negligible pigment concentrations (Johnsen et al., 2011), likely remained unnoticed. Detecting those groups would require a separate analysis, which was beyond the scope of this study. Lastly, Kohonen's self-organizing maps are strongly data-driven, making the output susceptible to input data quality and selection of explanatory variables. For our study, we maintained data quality using carefully curated input data. Moreover, correspondence between the retrieved bioregions, major hydrological patterns, and biogeochemical water properties in the area supports the robustness of the obtained division.

6. Conclusions

This study introduced a novel classification of the subarctic Pacific Ocean into five bioregions based on phytoplankton phenology metrics and functional groups, exploiting the satellite GlobColour time series and modern remote sensing capabilities to determine phytoplankton phenology and PFT during a more than 20-year period. The resulting bioregionalization shed new light on the variability within the subarctic Pacific, where the final five bioregions reflect significant differences in phytoplankton phenology patterns and community composition. In the Marginal and Archipelago bioregions, the spring diatom bloom was evident, and the Chl-*a* maxima were the highest due to the extra abundance of diatoms. In the Connecting bioregion, two blooms of similar magnitudes were observed, with relatively large variability in diatom abundance between years. The Central South and Central North bioregions mainly covered the Central Pacific and were dominated by green algae, haptophytes, and pelagophytes, less sensitive to iron depletion. The Chl-*a* seasonal cycle was less pronounced, with a predominance of fall blooms and large interannual variability. Generally, the bioregions overlap with the areas of intense mixing and physical transport offshore (Ueno et al., 2023) and coincide with surface patterns of iron and nutrient distribution (Nishioka et al., 2021). The spatial distribution of the bioregions underlines the importance of mesoscale processes across the subarctic Pacific Ocean (Ueno et al., 2023). Our study confirmed the pivotal role of iron and nutrient availability on the first trophic level, including phytoplankton phenology and structure, in addition to light limitation. Identifying bioregions is a critical first step towards understanding the large-scale spatial structure of phytoplankton communities that underpin the marine food web, with implications for zooplankton species composition and production and, subsequently, the entire food web. Further research should address the mechanisms controlling temporal dynamics within the bioregions. In the case of the subarctic Pacific, this has direct implications for foraging conditions available to salmon, the dominant nektonic consumer group in the region. Knowledge of spatial variability in food web properties can inform species and stock-specific life history experience, including potential for competition, and can also inform management decisions such as salmon hatchery production levels.

Funding

The work was funded by the British Columbia Salmon Restoration and Innovation Fund (BCSRIF) through the North Pacific Anadromous Fish Commission – the International Year of the Salmon Secretariat and Costa's NSERC Discovery Grant (RGPIN-2020-04042). The Copernicus Marine Service Evolution project GLOPHYTS (21036L05B-COP-INNO SCI-9000) funded contributions by HX and AB.

CRediT authorship contribution statement

Marta Konik: Conceptualization, Data curation, Formal analysis, Investigation, Methodology, Software, Validation, Visualization, Writing – original draft, Writing – review & editing. **M. Angelica Peña:** Conceptualization, Methodology, Supervision, Writing – review & editing. **Toru Hirawake:** Conceptualization, Supervision, Writing – review & editing, Methodology. **Brian P.V. Hunt:** Conceptualization, Methodology, Supervision, Writing – review & editing. **Perumthuruthil Suseelan Vishnu:** Methodology, Writing – review & editing. **Lisa B. Eisner:** Methodology, Writing – review & editing. **Astrid Bracher:** Funding acquisition, Methodology, Writing – review & editing. **Hongyan Xi:** Funding acquisition, Methodology, Writing – review & editing. **Christian Marchese:** Methodology, Writing – review & editing. **Maycira Costa:** Conceptualization, Funding acquisition, Methodology, Project administration, Resources, Supervision, Writing – review & editing.

Declaration of competing interest

The authors declare that they have no known competing financial interests or personal relationships that could have appeared to influence the work reported in this paper.

Data availability

Data will be made available on request.

Acknowledgements

We thank the colleagues and the crews of *R/V Sir John Franklin*, *R/V Bell M. Shimada*, and *R/V TINRO* for collecting the *in situ* samples during the International Year of the Salmon High-Seas Expeditions.

This study was conducted using E.U. Copernicus Marine Service Information: https://doi.org/10.48670/moi-00099 and GlobColour data (http://globcolour.info) developed, validated, and distributed by ACRI-ST, France. Data from the monitoring stations along Line-P were available thanks to the courtesy of Fisheries and Oceans Canada (*https://open.canada.ca/data/en/dataset/8c630c40-a40f-42be-b5e1-e7ade5d560e5*).

The R scripts for the EOF-based PFT retrieval models were adapted from Marc Taylor's original version.

Appendix A. Supplementary material

Supplementary data to this article can be found online at https://doi.org/10.1016/j.pocean.2024.103315.

References

Abe, S., Nakamura, T., 2013. Processes of breaking of large-amplitude unsteady lee waves leading to turbulence. J. Geophys. Res. Oceans 118, 316–331. https://doi.org/10.1029/2012JC008160.

ACRI-ST, GlobColour Team, Mangin, A., Fanton d'Andon, O., 2017. GlobColour Product User, Guide, GC-UM-ACR-PUG-01, Version 4.1 Sophia-Antipolis..

Alvain, S., Moulin, C., Dandonneau, Y., Bréon, F.M., 2005. Remote sensing of phytoplankton groups in case 1 waters from global SeaWiFS imagery. Deep-Sea Res. I 52, 1989–2004. https://doi.org/10.1016/j.dsr.2005.06.015.

Alvain, S., Moulin, C., Dandonneau, Y., Loisel, H., 2008. Seasonal distribution and succession of dominant phytoplankton groups in the global ocean: A satellite view. Global Biogeochem. Cycles 22, GB3001. https://doi.org/10.1029/2007GB003154.

Anderson, T.R., 2005. Plankton functional type modelling: running before we can walk? J. Plankton Res. 27 (11), 1073–1081. https://doi.org/10.1093/plankt/fbi076.

Ayers, J.M., Lozier, M.S., 2010. Physical controls on the seasonal migration of the North Pacific transition zone chlorophyll front. J. Geophys. Res. 115, C05001. https://doi.org/10.1029/2009JC005596.

Bailey, S.W., Werdell, P.J., 2006. A multi-sensor approach for the on-orbit validation of ocean color satellite data products. Remote Sens. Environ. 1021–2, 12–23. https://doi.org/10.1016/j.rse.2006.01.015.

Bendriem, N., Roman, R., Gibson, D., Sumaila, U.R., 2019. A review of the fate of southern British Columbia Coho salmon over time. Fish. Res. 218, 10–21. https://doi.org/10.1016/j.fishres.2019.04.002.

Boelaert, J., Ollion, E., Sodoge, J., Megdoud, M., Naji, O., Kote, A.L., Renoud, T., Hym, S. 2021. aweSOM: Interactive Self-Organizing Maps. R-cran package, https://cran.r-project.org/package=aweSOM.

Booth, B.C., Lewin, J., Postel., J.R. 1993. Temporal variation in the structure of autotrophic and heterotrophic communities in the subarctic Pacific. Progress in Oceanography, 32, 57 – 99, doi: 10.1016/0079-66119390009-3.

Bracher, A., Bouman, H.A., Brewin, R.J.W., Bricaud, A., Brotas, V., Ciotti, A.M., Clementson, L., Devred, E., Di Cicco, A., Dutkiewicz, S., Hardman-Mountford, N.J., Hickman, A.E., Hieronymi, M., Hirata, T., Losa, S.N., Mouw, C.B., Organelli, E., Raitsos, D.E., Uitz, J., Vogt, M., Wolanin, A., 2017. Obtaining phytoplankton diversity from ocean color: A scientific roadmap for future development. Front. Mar. Sci. 455 https://doi.org/10.3389/fmars.2017.00055.

Brewin, R.J.W., Sathyendranath, S., Jackson, T., Barlow, R., Brotas, V., Airs, R., Lamont, T., 2015. Influence of light in the mixed-layer on the parameters of a three-component model of phytoplankton size class. Remote Sens. Environ. 168, 437–450. https://doi.org/10.1016/j.rse.2015.07.004.

Britten, G.L., Padalino, C., Forget, G., Follows, M.J., 2022. Seasonal photoacclimation in the North Pacific Transition Zone. Global Biogeochem. Cycles 36, e2022GB007324. https://doi.org/10.1029/2022GB007324.

Brody, S.R., Lozier, M.S., Dunne, J.P., 2013. A comparison of methods to determine phytoplankton bloom initiation. J. Geophys. Res. Oceans 118, 2345–2357. https://doi.org/10.1002/jgrc.20167.

Brugger, D., Bogdan, M., Rosenstiel, W., 2008. Automatic cluster detection in Kohonen's SOM. IEEE Trans. Neural Netw. 193 https://doi.org/10.1109/TNN.2007.909556.

Brzezinski, M.A., Varela, D.E., Jenkins, B.D., Buck, K.N., Kafrissen, S.M., Jones, J.L., 2022. The upper ocean silicon cycle of the subarctic Pacific during the EXPORTS field campaign. Elem. Sci. Anth. 101 https://doi.org/10.1525/elementa.2021.00087.

Burger, J., Gochfeld, M., Niles, L., Powers, C., Brown, K., Clarke, J., Dey, A., Kosson, D., 2015. Complexity of bioindicator selection for ecological, human, and cultural health: Chinook salmon and red knot as case studies. Environ. Monit. Assess. 187102 https://doi.org/10.1007/s10661-014-4233-4.

Burnham, K.P., Anderson, D.R., Huyvaert, K.P., 2011. AIC model selection and multimodel inference in behavioral ecology: some background, observations, and comparisons. Behav. Ecol. Sociobiol. 65, 23–35. https://doi.org/10.1007/s00265-010-1029-6.

Burt, W.J., Westberry, T.K., Behrenfeld, M.J., Zeng, C., Izett, R.W., Tortell, P.D., 2018. Carbon: Chlorophyll ratios and net primary productivity of subarctic Pacific surface waters derived from autonomous shipboard sensors. Global Biogeochem. Cycles 32 (267–288), 2018. https://doi.org/10.1002/2017GB005783.

Buttlar, J.V., Zscheischler, J., Mahecha, M.D., 2014. An extended approach for spatio-temporal gap filling: Dealing with large and systematic gaps in geoscientific datasets. Nonlinear Processes Geophys. 21, 203–215. https://doi.org/10.5194/npg-21-203-2014.

Charrad, M., Ghazzali, N., Boiteau, V., Niknafs, A., 2014. NbClust: an R package for determining the relevant number of clusters in a data set. J. Stat. Softw. 61 (6), 1–36. https://doi.org/10.18637/jss.v061.i06.

Chase, A.P., Kramer, S.J., Haëntjens, N., Boss, E.S., Karp-Boss, L., Edmondson, M., Graff, J.R., 2020. Evaluation of diagnostic pigments to estimate phytoplankton size classes. Limnol. Oceanogr. Methods 18 (10), 570–584. https://doi.org/10.1002/lom3.10385.

Chittenden, C.M., Beamish, R.J., McKinley, R.S., 2009. A critical review of Pacific salmon marine research relating to climate. ICES J. Mar. Sci. 66, 2195–2204.

Ciavatta, S., Kay, S., Brewin, R.J.W., Cox, R., Di Cicco, A., Nencioli, F., Polimene, L., Sammartino, M., Santoleri, R., Skákala, J., Tsapakis, M., 2019. Ecoregions in the Mediterranean Sea through the reanalysis of phytoplankton functional types and carbon fluxes. J. Geophys. Res. Oceans 124, 6737–6759. https://doi.org/10.1029/2019JC015128.

Claiborne, A.M., Campbell, L., Stevick, B., Sandell, T., Losee, J.P., Litz, M., Anderson, J. H., 2021. Correspondence between scale growth, feeding conditions, and survival of adult Chinook salmon returning to Puget Sound and coastal Washington: Implications for forecasting. Prog. Oceanogr. 198, 102443 https://doi.org/10.1016/j.pocean.2020.102443.

Cole, H., Henson, S., Martin, A., Yool, A., 2012. Mind the gap: The impact of missing data on the calculation of phytoplankton phenology metrics. J. Geophys. Res. 117, C08030. https://doi.org/10.1029/2012JC008249.

Concha, J.A., Bracaglia, M., Brando, V.E., 2021. Assessing the influence of different validation protocols on Ocean Colour match-up analyses. Remote Sens. Environ. 259, 112415 https://doi.org/10.1016/j.rse.2021.112415.

Crusius, J., Schroth, A.W., Resing, J.A., Cullen, J., Campbell, R.W., 2017. Seasonal and spatial variabilities in northern Gulf of Alaska surface water iron concentrations driven by shelf sediment resuspension, glacial meltwater, a Yakutat eddy, and dust. Global Biogeochem. Cycles 31, 942–960. https://doi.org/10.1002/2016GB005493.

Crusius, J. 2021. Dissolved Fe supply to the central Gulf of Alaska is inferred to be derived from Alaskan glacial dust that is not resolved by dust transport models. Journal of Geophysical Research: Biogeosciences, 126, e2021JG006323, doi: org/10.1029/2021JG006323.

Cullen, J.T., Chong, M., Ianson, D., 2009. British Columbian continental shelf as a source of dissolved iron to the subarctic northeast Pacific Ocean. Global Biogeochem. Cycles 23, GB4012. https://doi.org/10.1029/2008GB003326.

Cushing, D.H., 1990. Plankton production and year-class strength in fish populations: An update of the match/mismatch hypothesis. Adv. Mar. Biol. 26, 249–293. https://doi.org/10.1016/S0065-28810860202-3.

Davis, K.A., Banas, N.S., Giddings, S.N., Siedlecki, S.A., MacCready, P., Lessard, E.J., Kudela, R.M., Hickey, B.M., 2014. Estuary-enhanced upwelling of marine nutrients fuels coastal productivity in the U.S. Pacific Northwest. J. Geophys. Res. Oceans 119, 8778–8799. https://doi.org/10.1002/2014JC010248.

Del Bel Belluz, J., Peña, M.A., Jackson, J.M., Nemcek, N., 2021. Phytoplankton Composition and Environmental Drivers in the Northern Strait of Georgia (Salish Sea), British Columbia, Canada. Estuaries and Coasts 44, 1419–1439. https://doi.org/10.1007/s12237-020-00858-2.

Dinno, A., 2015. Nonparametric pairwise multiple comparisons in independent groups using Dunn's test. Stata J. 151, 292–300. https://doi.org/10.1177/1536867X1501500117.

Eisner, L.B., Lomas, M.W. 2022. Flow cytometry data from the R/V TINRO, NOAA Bell M. Shimada and CCGS Sir John Franklin during the 2022 International Year of the Salmon Pan-Pacific Winter High Seas Expedition . North Pacific Anadromous Fish Commission, doi: 10.21966/j26w-by50.

Elizondo, U.H., Righetti, D., Benedetti, F., Vogt, M., 2021. Biome partitioning of the global ocean based on phytoplankton biogeography. Prog. Oceanogr. 194, 102530 https://doi.org/10.1016/j.pocean.2021.102530.

Fendereski, F., Vogt, M., Payne, M.R., Lachkar, Z., Gruber, N., Salmanmahiny, A., Hosseini, S.A., 2014. Biogeographic classification of the Caspian Sea. Biogeosciences 11, 6451–6470. https://doi.org/10.5194/bg-11-6451-2014.

Feng, J., Li, D., Zhang, J., Zhao, L., 2022. Variations and environmental controls of primary productivity in the Amundsen Sea. Front. Mar. Sci. 9, 891663 https://doi.org/10.3389/fmars.2022.891663.

Fiechter, J., Moore, A.M., Edwards, C.A., Bruland, K.W., Di Lorenzo, E., Lewis, C.V.W., Powell, T.M., Curchitser, E.N., Hedstrom, K., 2009. Modeling iron limitation of primary production in the coastal Gulf of Alaska. Deep-Sea Res. II 56, 2503–2519. https://doi.org/10.1016/j.dsr2.2009.02.010.

Fujiki, T., Matsumoto, K., Honda, M.C., Hawakami, H., Wanatabe, S., 2009. Phytoplankton composition in the subarctic North Pacific during autumn 2005. J. Plankton Res. 312, 179–191. https://doi.org/10.1093/plankt/fbn108.

Fujiki, T., Matsumoto, K., Mino, Y., Sasaoka, K., Wakita, M., Kawakami, H., Honda, M.C., Watanabe, S., Saino, T., 2014. Seasonal cycle of phytoplankton community structure and photophysiological state in the western subarctic gyre of the North Pacific. Limnol. Oceanogr. 593, 887–900. https://doi.org/10.4319/lo.2014.59.3.0887.

GEBCO, Compilation Group, 2022. GEBCO_2022 Grid. https://doi.org/10.5285/e0f0bb80-ab44-2739-e053-6c86abc0289c.

Giannini, F., Hunt, B.P.V., Jacoby, D., Costa, M., 2021. Performance of OLCI Sentinel-3A satellite in the Northeast Pacific coastal waters. Remote Sens. Environ. 256, 112317 https://doi.org/10.1016/j.rse.2021.112317.

Gieskes, W.W.C., Kraay, G.W., Nontli, A., Setiapermana, D., Sutomo, 1988. Monsoonal alternation of a mixed and a layered structure in the phytoplankton of the euphotic zone of the Banda Sea (Indonesia): A mathematical analysis of algal fingerprints. Neth. J. Sea Res. 223, 123–133.

Goes, J.I., Sasaoka, K., Gomes, H.d.R., Saitoh, S.-I., Saino, T., 2004. A comparison of the seasonality and interannual variability of phytoplankton biomass and production in the Western and Eastern Gyres of the subarctic Pacific using multi-sensor satellite data. J. Oceanogr. 60, 75–91. https://doi.org/10.1023/B:JOCE.0000038320.94273.25.

Golub, G.H., Kahan, W., 1965. Calculating the singular values and pseudo-inverse of a matrix. Journal of the Society for Industrial and Applied Mathematics, Series b: Numerical Analysis. 22, 205–224. https://doi.org/10.1137/0702016.

Graham, C., Pakhomov, E., Hunt, B., 2020. A salmon diet database for the North Pacific Ocean. Figshare Collection. https://doi.org/10.6084/m9.figshare.c.4974128.v1.

Hastie, T.J., Pregibon, D., 1992. Generalized linear models. In: Chambers, S.J.M., Hastie, T.J. (Eds.), Statistical Models in S. Routledge, New York, pp. 195–247.

Hayakawa, M., Suzuki, K., Saito, H., Takahashi, K., Ito, S., 2008. Differences in cell viabilities of phytoplankton between spring and late summer in the northwest Pacific Ocean. J. Exp. Mar. Biol. Ecol. 360, 63–70.

Head, E. 2002. Pigment data of site BAF89/3-5. doi:10.1594/PANGAEA.67729.

Healey, M.C., Thomson, K.A., Leblond, P.H., Huato, L., Hinch, S.G., Walters, C.J., 2000. Computer simulations of the effects of the Sitka eddy on the migration of sockeye salmon returning to British Columbia. Fish. Oceanogr. 93, 271–281. https://doi.org/10.1046/j.1365-2419.2000.00135.x.

Higgins, H., Wright, S., Schlüter, L., 2011. Quantitative interpretation of chemotaxonomic pigment data. In: Roy, S., Llewellyn, C., Egeland, E., Johnsen, G. (Eds.), Phytoplankton Pigments: Characterization, Chemotaxonomy and Applications in Oceanography Cambridge Environmental Chemistry Series. Cambridge University Press, Cambridge, pp. 257–313. https://doi.org/10.1017/CBO9780511732263.010.

Hilborn, A., Devred, E., 2022. Delineation of eastern Beaufort Sea sub-regions using self-organizing maps applied to 17 years of MODIS-Aqua data. Front. Mar. Sci. 9 (1–19), 912865 https://doi.org/10.3389/fmars.2022.912865.

Hirata, T., Aiken, J., Hardman-Mountford, N., Smyth, T.J., Barlow, R., 2008. An absorption model to determine phytoplankton size classes from satellite ocean colour. Remote Sens. Environ. 112, 3153–3159.

Hirata, T., Hardman-Mountford, N., Brewin, R., Aiken, J., Barlow, R., Suzuki, K., Isada, T., Howell, E., Hashioka, T., Noguchi-Aita, M., Yamanaka, Y., 2011. Synoptic relationships between surface Chlorophyll-a and diagnostic pigments specific to phytoplankton functional types. Biogeosciences 8, 311–327. https://doi.org/10.5194/bg-8-311-2011.

Hjort, J., 1926. Fluctuations in the year classes of important food fishes. ICES J. Mar. Sci. 1, 5–38. https://doi.org/10.1093/icesjms/1.1.5.

Honkanen, H.M., Boylan, P., Dodd, J.A., Adams, C.E., 2019. Life stage-specific, stochastic environmental effects overlay density dependence in an Atlantic salmon population. Ecol. Freshw. Fish 28, 156–166. https://doi.org/10.1111/eff.12439.

Hunt Jr, G.L., Stabeno, P.J., 2005. Oceanography and ecology of the Aleutian Archipelago: Spatial and temporal variation. Fish. Oceanogr. 14 (Suppl. 1), 292–306. https://doi.org/10.1111/j.1365-2419.2005.00378.x.

Isada, T., Kuwata, A., Saito, H., Ono, T., Ishii, M., Yoshikawa-Inoue, H., Suzuki, K., 2009. Photosynthetic features and primary productivity of phytoplankton in the Oyashio

and Kuroshio-Oyashio transition regions of the northwest Pacific. J. Plankton Res. 319, 1009–1025. https://doi.org/10.1093/plankt/fbp050.
Isada, T., Hattori-Saito, A., Saito, H., Kondo, Y., Nishioka, J., Kuma, K., Hattori, H., McKay, R.M.L., Suzuki, K., 2019. Responses of phytoplankton assemblages to iron availability and mixing water masses during the spring bloom in the Oyashio region, NW Pacific. Limnol. Oceanogr. 64, 197–216. https://doi.org/10.1002/lno.11031.
Isles, P.D.F., Pomati, F., 2021. An operational framework for defining and forecasting phytoplankton blooms. Front. Ecol. Environ. 19 (8), 443–450. https://doi.org/10.1002/fee.2376.
Isoguchi, O., Kawamura, H., Oka, E., 2006. Quasi-stationary jets transporting surface warm waters across the transition zone between the subtropical and the subarctic gyres in the North Pacific. J. Geophys. Res. 111, C10003. https://doi.org/10.1029/2005JC003402.
Jeffrey, S.W., Wright, S.W. 2006. Photosynthetic Pigments in Marine Microalgae. In: Subba Rao, D.V. (Ed.), Algal Cultures, Analogues of Blooms and Applications, Science Publishers Enfield, pp. 33–90, NH, USA, ISBN: 1-57808-393-1.
Johnsen, G., Moline, M., Pettersson, L., Pinckney, J., Pozdnyakov, D., Egeland, E., Schofield, O., 2011. Optical monitoring of phytoplankton bloom pigment signatures. In: Roy, S., Llewellyn, C., Egeland, E., Johnsen, G. (Eds.), Phytoplankton Pigments: Characterization, Chemotaxonomy and Applications in Oceanography Cambridge Environmental Chemistry Series. Cambridge University Press, Cambridge, pp. 538–606. https://doi.org/10.1017/CBO9780511732263.020.
Kléparski, L., Beaugrand, G., Edwards, M., 2021. Plankton biogeography in the North Atlantic Ocean and its adjacent seas: Species assemblages and environmental signatures. Ecol. Evol. 11, 5135–5149. https://doi.org/10.1002/ece3.7406.
Kohonen, T., 2013. Essentials of the self-organizing map. Neural Netw. 37, 52–65. https://doi.org/10.1016/j.neunet.2012.09.018.
Kramer, S.J., Siegel, D.A., 2019. How can phytoplankton pigments be best used to characterize surface ocean phytoplankton groups for ocean color remote sensing algorithms? J. Geophys. Res. Oceans 124, 7557–7574. https://doi.org/10.1029/2019JC015604.
Krug, L.A., Platt, T., Sathyendranath, S., Barbosa, A.B., 2018. Patterns and drivers of phytoplankton phenology off SW Iberia: A phenoregion based perspective. Prog. Oceanogr. 165, 233–256. https://doi.org/10.1016/j.pocean.2018.06.010.
Laufkötter, C., Vogt, M., Gruber, N., 2013. Long-term trends in ocean plankton production and particle export between 1960–2006. Biogeosciences 10, 7373–7393. https://doi.org/10.5194/bg-10-7373-2013.
Lavigne, L., Civitarese, G., Gačić, M., D'Ortenzio, F., 2018. Impact of decadal reversals of the north Ionian circulation on phytoplankton phenology. Biogeosciences 15, 4431–4445. https://doi.org/10.5194/bg-15-4431-2018.
Le Quéré, C., Harrison, S.P., Prentice, I.C., Buitenhuis, E.T., Aumont, O., Bopp, L., Claustre, H., Cotrim Da Cunha, L., Geider, R., Giraud, X., Klaas, C., Kohfeld, K.E., Legendre, L., Manizza, M., Platt, T., Rivkin, R.B., Sathyendranath, S., Uitz, J., Watson, A.J., Wolf-Gladrow, D., 2005. Ecosystem dynamics based on plankton functional types for global ocean biogeochemistry models. Glob. Chang. Biol. 11, 2016–2041.
Lee, J.A., Verleysen, M. 2007. Nonlinear Dimensionality Reduction. Springer Science+ Business Media, LLC, Springer, New York, eBook ISBN: 978-0-387-39351-3.
Letelier, R. 2007. "Phytoplankton." Ocean Carbon and Biogeochemistry Data System. OCB DMO, WHOI. Accessed: '03/2022'. http://globec.whoi.edu/jg/dir/globec/nep/ccs/process/.
Liu, H., Suzuki, K., Minami, C., Saino, T., Watanabe, M., 2002. Picoplankton community structure in the subarctic Pacific Ocean and the Bering Sea during summer 1999. Mar. Ecol. Prog. Ser. 237, 1–14.
Liu, H., Suzuki, K., Saito, H., 2004. Community structure and dynamics of phytoplankton in the Western subarctic Pacific Ocean: A synthesis. J. Oceanogr. 60, 119–137.
Longhurst, A., Sathyendranath, S., Platt, T., Caverhill, C., 1995. An estimate of global primary production in the ocean from satellite radiometer data. J. Plankton Res. 17, 1245–1271.
Mackey, M.D., Higgins, H.W., Mackey, D.J., Wright, S.W. 1997. CHEMTAX user's manual: a program for estimating class abundances from chemical markers — application to HPLC measurements of phytoplankton pigments. CSIRO Marine Laboratories Report, 229, 47 pp., Hobart, Australia, ISBN: 0 643 06040 5.
Mackey, M.D., Mackey, D.J., Higgins, H.W., Wright, S.W., 1996. CHEMTAX - a program for estimating class abundances from chemical markers: Application to HPLC measurements of phytoplankton. Mar. Ecol. Prog. Ser. 144, 265–283.
Mamat, A.R., Mohamed, F.S., Mohamed, M.A., Rawi, N.M., Awang, M.I., 2018. Silhouette index for determining optimal k-means clustering on images in different color models. International Journal of. Eng. Technol. 7 (2.14), 105–109. https://doi.org/10.14419/ijet.v7i2.14.11464.
Marchese, C., Albouy, C., Tremblay, J.É., Dumont, D., D'Ortenzio, F., Vissault, S., Bélanger, S., 2017. Changes in phytoplankton bloom phenology over the North Water (NOW) polynya: a response to changing environmental conditions. Polar Biol. 40, 1721–1737. https://doi.org/10.1007/s00300-017-2095-2.
Marchese, C., Castro de la Guardia, L., Myers, P.G., Bélanger, S., 2019. Regional differences and inter-annual variability in the timing of surface phytoplankton blooms in the Labrador Sea. Ecol. Ind. 96 (1), 81–90. https://doi.org/10.1016/j.ecolind.2018.08.053.
Marchese, C., Hunt, B.P.V., Giannini, F., Ehrler, M., Costa, M., 2022. Bioregionalization of the coastal and open oceans of British Columbia and Southeast Alaska based on Sentinel-3A satellite-derived phytoplankton seasonality. Front. Mar. Sci. 9, 968470 https://doi.org/10.3389/fmars.2022.968470.
McKinnell, S., Irvine, J.R., 2021. Phenology and Fraser River sockeye salmon marine survival. Prog. Oceanogr. 197102632 https://doi.org/10.1016/j.pocean.2021.102632.
Mizuno, Y., Nishioka, J., Tanaka, T., Tada, Y., Suzuki, K., Tsuzuki, Y., Sugimoto, A., Yamashita, Y., 2018. Determination of the freshwater origin of Coastal Oyashio Water using humic-like fluorescence in dissolved organic matter. J. Oceanogr. 74, 509–521. https://doi.org/10.1007/s10872-018-0477-x.
Mochizuki, M., Shiga, N., Saito, M., Imai, K., Nojiri, Y., 2002. Seasonal changes in nutrients, chlorophyll a and the phytoplankton assemblage of the western subarctic gyre in the Pacific Ocean. Deep-Sea Res. II 49, 5421–5439. https://doi.org/10.1016/S0967-06450200209-6.
Moisan, T.A., Rufty, K.M., Moisan, J.R., Linkswiler, M.A., 2017. Satellite observations of phytoplankton functional type spatial distributions, phenology, diversity, and ecotones. Front. Mar. Sci. 4189 https://doi.org/10.3389/fmars.2017.00189.
Morel, A., Gentili, B., Claustre, H., Babin, M., Bricaud, A., Ras, J., Tieche, F., 2007. Optical properties of the "clearest" natural waters. Limnol. Oceanogr. 52 (1), 217–229. https://doi.org/10.4319/lo.2007.52.1.0217.
Mouw, C.B., Hardman-Mountford, N.J., Alvain, S., Bracher, A., Brewin, R.J.W., Bricaud, A., Ciotti, A.M., Devred, E., Fujiwara, A., Hirata, T., Hirawake, T., Kostadinov, T.S., Roy, S., Uitz, J., 2017. A consumer's guide to satellite remote sensing of multiple phytoplankton groups in the global ocean. Front. Mar. Sci. 4, 41. https://doi.org/10.3389/fmars.2017.00041.
Murtagh, F., Legendre, P., 2014. Ward's hierarchical agglomerative clustering method: which algorithms implement Ward's criterion? J. Classif. 31, 274–295. https://doi.org/10.1007/s00357-014-9161-z.
Myers, K.W., Irvine, J.R., Logerwell, E.A., Urawa, S., Naydenko, S.V., Zavolokin, A.V., Davis, N.D. 2016. Pacific salmon and steelhead: Life in a changing winter ocean. In: Urawa, S., Trudel, M., Beamish, R.J., Farley Jr., E.V., Guyon, J.R., Irvine, J.R., Saito, T., Zavolokin, A.V., Temnykh, O.S., Davis, N.D. (eds.), Pacific Salmon and Steelhead Production in a Changing Climate: Past, Present, and Future. North Pacific Anadromous Fish Commission, Bulletin No 6, 113–138, doi: 10.23849/npafcb6/113–138.
Naidenko, S.V., 2001. Interannual dynamics of the trophic structure of zooplankton of the southern Kuril region. Russ. J. Mar. Biol. 275, 282–290. https://doi.org/10.1023/A:1012596429696.
Nakamura, T., Awaji, T., Hatayama, T., Akitomo, K., Takizawa, T., Kono, T., Kawasaki, Y., Fukasawa, M., 2000. The generation of large-amplitude unsteady lee waves by subinertial K1 tidal flow: A possible vertical mixing mechanism in the Kuril Straits. J. Phys. Oceanogr. 30, 1601–1621. https://doi.org/10.1175/1520-04852000030<1601:TGOLAU>2.0.CO;2.
Nemcek, N., Peña, M.A. 2014. Institute of Ocean Sciences protocols for phytoplankton pigment analysis by HPLC. Canadian technical report of fisheries and aquatic sciences, 3117, https://waves-vagues.dfo- mpo.gc.ca/Library/356308.pdf.
Nishioka, J., Obata, H., Ogawa, H., Ono, K., Yamashita, Y., Lee, K., Takeda, S., Yasuda, I., 2020. Subpolar marginal seas fuel the North Pacific through the intermediate water at the termination of the global ocean circulation. PNAS 11723, 12665–12673. https://doi.org/10.1073/pnas.2000658117.
Nishioka, J., Obata, H., Hirawake, T., Kondo, Y., Yamashita, Y., Misumi, K., Yasuda, I., 2021. A review: Iron and nutrient supply in the subarctic Pacific and its impact on phytoplankton production. J. Oceanogr. 77, 561–587. https://doi.org/10.1007/s10872-021-00606-5.
NOAA, National Centers for Environmental Information/NESDIS/NOAA/U.S., Department of Commerce, 2007. NOAA Optimum Interpolation 1/4 Degree Daily Sea Surface Temperature Analysis. Research Data Archive at the National Center for Atmospheric Research, Computational and Information Systems Laboratory 2022. https://doi.org/10.5065/EM0T-1D34. Accessed: August 29th.
Obayashi, Y., Tanoue, E., Suzuki, K., Handa, N., Nojiri, Y., Wong, C.S., 2001. Spatial and temporal variabilities of phytoplankton community structure in the northern North Pacific as determined by phytoplankton pigments. Deep-Sea Res. I 48, 439–469.
Okamoto, S., Hirawake, T., Saitoh, S.-I., 2010. Interannual variability in the magnitude and timing of the spring bloom in the Oyashio region. Deep-Sea Res. II 57, 1608–1617. https://doi.org/10.1016/j.dsr2.2010.03.005.
O'Reilly, J.E., Werdell, P.J., 2019. Chlorophyll algorithms for ocean color sensors - OC4, OC5 & OC6. Remote Sens. Environ. 229, 32–47. https://doi.org/10.1016/j.rse.2019.04.021.
Pahlevan, N., Smith, B., Schalles, J., Binding, C., Cao, Z., Ma, R., Alikas, K., Kangro, K., Gurlin, D., Hà, N., Matsushita, B., Moses, W., Greb, S., Lehmann, M.K., Ondrusek, M., Oppelt, N., Stumpf, R., 2020. Seamless retrievals of chlorophyll-a from Sentinel-2 MSI and Sentinel-3 OLCI in inland and coastal waters: A machine-learning approach. Remote Sens. Environ. 240, 111604 https://doi.org/10.1016/j.rse.2019.111604.
Pan, X., Mannino, A., Marshall, H.G., Filippino, K.C., Mulholland, M.R., 2011. Remote sensing of phytoplankton community composition along the northeast coast of the United States. Remote Sens. Environ. 115, 3731–3747. https://doi.org/10.1016/j.rse.2011.09.011.
Pearcy, W.G., 1991. Biology of the Transition Region. In: Wetherall, J.H. (Ed.), Biology, Oceanography and Fisheries of the North Pacific Transition Zone and the Subarctic Frontal Zone. NOAA Technical Report NMFS 105, u.s. Department of Commerce.
Peloquin, J.M., Swan, C., Gruber, N., Vogt, M., Claustre, H., Ras, J., Uitz, J., Barlow, R.G., Behrenfeld, M.J., Bidigare, R.R., Dierssen, H.M., Ditullio, G., Fernández, E., Gallienne, C., Gibb, S.W., Goericke, R., Harding, L., Head, E.J.H., Holligan, P.M., Hooker, S.B., Karl, D., Landry, M.R., Letelier, R., Llewellyn, C., Lomas, M.W., Lucas, M., Mannino, A., Marty, J.-C., Mitchell, B.G., Muller-Karger, F.E., Nelson, N., O'Brien, C.J., Prezelin, B., Repeta, D.J., Smith Jr., W.O., Smythe-Wright, D., Stumpf, R., Subramaniam, A., Suzuki, K., Trees, C., Vernet, M., Wasmund, N., Wright, S., 2013. The MAREDAT global database of high performance liquid chromatography marine pigment measurements - Gridded data product NetCDF - Contribution to the MAREDAT World Ocean Atlas of Plankton Functional Types. PANGAEA. https://doi.org/10.1594/PANGAEA.793246.

Peña, M.A., Nemcek, N., Robert, M., 2019. Phytoplankton responses to the 2014–2016 warming anomaly in the northeast subarctic Pacific Ocean. Limnol. Oceanogr. 64, 515–525. https://doi.org/10.1002/lno.11056.

Peperzak, L., Zetsche, E.M., Gollasch, S., Artigas, L.F., Bonato, S., Creach, V., de Vrég, P., Dubelaar, G.B.J., Henneghieni, J., Hess-Ergaj, O.-K., Langelaar, R., Larsen, A., Maurerm, B.N., Mosselaar, A., Reavie, E.D., Rijkeboer, M., Tobiesen, A., 2018. Comparing flow cytometry and microscopy in the quantification of vital aquatic organisms in ballast water. Journal of Marine Engineering and Technology 19 (2), 68–77. https://doi.org/10.1080/20464177.2018.1525806.

Phillips, S.R., Costa, M., 2017. Spatial-temporal bio-optical classification of dynamic semi-estuarine waters in western North America. Estuar. Coast. Shelf Sci. 199: 35e48 https://doi.org/10.1016/j.ecss.2017.09.029.

Pinkney, J. 2010. The USC method [In:] Hooker, S.B., Thomas, C.S., Van Heukelem, L., Schlüter, L., Russ, M.E., Ras, J., Claustre, H., Clementson, L., Canuti, E., Berthon, J-F., Perl, J., Normandeau, C., Cullen, J., Kienast, M., Pinckney, J.L. The Fourth SeaWiFS HPLC Analysis Round-Robin Experiment SeaHARRE-4. NASA/TM–2010–215857. National Aeronautics and Space Administration, Goddard Space Flight Center, Greenbelt, Maryland, Chapter 11.

Platt, T., Sathyendranath, S., 1988. Oceanic primary production: Estimation by remote sensing at local and regional scales. Science 2414873, 1613–1620. https://doi.org/10.1126/science.241.4873.1613.

Polovina, J.J., Howell, E., Kobayashi, D.R., Seki, M.P., 2001. The transition zone chlorophyll front, a dynamic global feature defining migration and forage habitat for marine resources. Prog. Oceanogr. 49, 469–483.

Polovina, J.J., Howell, E.A., Kobayashi, D.R., Seki, M.P., 2017. The transition zone chlorophyll front updated: Advances from a decade of research. Prog. Oceanogr. 150, 79–85. https://doi.org/10.1016/j.pocean.2015.01.006.

Pramlall, S., Jackson, J.M., Konik, M., Costa, M., 2023. Merged multi-sensor ocean colour chlorophyll product evaluation for the British Columbia coast. Remote Sens. (Basel) 15 (3), 687. https://doi.org/10.3390/rs15030687.

R Core Team, 2018. R: A Language and Environment for Statistical Computing. R Foundation for Statistical Computing, Vienna, Austria. Available online at https://www.R-project.org/.

Racault, M.-F., Le Quéré, C., Buitenhuis, E., Sathyendranath, S., Platt, T., 2012. Phytoplankton phenology in the global ocean. Ecol. Ind. 14, 152–163. https://doi.org/10.1016/j.ecolind.2011.07.010.

Rathbun, S., 1998. Spatial modelling in irregularly shaped regions: Kriging estuaries. Environmetrics 9, 109–129. https://doi.org/10.1002/SICI1099-095X199803/049:2<109::AID-ENV279>3.0.CO;2-L.

Reynolds, R.W., Rayner, N.A., Smith, T.M., Stokes, D.C., Wang, W., 2002. An improved in situ and satellite SST analysis for climate. J. Clim. 15, 1609–1625.

Reynolds, A.P., Richards, G., Rayward-Smith, V.J., 2004. The application of K-Medoids and PAM to the clustering of rules. Lect. Notes Comput. Sci 173–178. https://doi.org/10.1007/978-3-540-28651-6_25.

Reynolds, R.W., Smith, T.M., Liu, C., Chelton, D.B., Casey, K.S., Schlax, M.G., 2007. Daily high-resolution blended analyses for sea surface temperature. J. Clim. 20, 5473–5496. https://doi.org/10.1175/2007JCLI1824.1.

Roden, G.I., 1991. Subarctic-subtropical transition zone of the North Pacific: Large-scale aspects and mesoscale structure. In: Wetherall, J.H. (Ed.), Biology, Oceanography and Fisheries of the North Pacific Transition Zone and the Subarctic Frontal Zone. NOAA Technical Report NMFS 105, u.s. Department of Commerce.

Rosengard, S.Z., Freshwater, C., McKinnell, S., Xu, Y., Tortell, P.D., 2021. Covariability of Fraser River sockeye salmon productivity and phytoplankton biomass in the Gulf of Alaska. Fish. Oceanogr. 30, 666–678. https://doi.org/10.1111/fog.12544.

Rousseeuw, P., 1987. Silhouettes: a graphical aid to the interpretation and validation of cluster analysis. J. Comput. Appl. Math. 20, 53–65. https://doi.org/10.1016/0377-0427(87)90125-7.

Rovegno, P.S., Edwards, C.A., Bruland, K.W., 2009. Observations of a Kenai eddy and a Sitka eddy in the Northern Gulf of Alaska. J. Geophys. Res. 114, C11012. https://doi.org/10.1029/2009JC005451.

Sarthou, G., Timmermans, K.R., Blain, S., Tréguer, P., 2005. Growth physiology and fate of diatoms in the ocean: a review. J. Sea Res. 53, 25–42. https://doi.org/10.1016/j.seares.2004.01.007.

Sasaoka, K., Chiba, S., Saino, T., 2011. Climatic forcing and phytoplankton phenology over the subarctic North Pacific from 1998 to 2006, as observed from ocean color data. Geophys. Res. Lett. 38, L15609. https://doi.org/10.1029/2011GL048299.

Schlitzer, R., 2021. Ocean Data View, https://odv.awi.de.

Schuback, N., Schallenberg, C., Duckham, C., Maldonado, M.T., Tortell, P.D., 2015. Interacting Effects of Light and Iron Availability on the Coupling of Photosynthetic Electron Transport and CO_2-Assimilation in Marine Phytoplankton. PLoS One 10 (7), e0133235.

Shiozaki, T., Ito, S.-I., Takahashi, K., Saito, H., Nagata, T., Furuya, K., 2014. Regional variability of factors controlling the onset timing and magnitude of spring algal blooms in the northwestern North Pacific. J. Geophys. Res. Oceans 119, 253–265. https://doi.org/10.1002/2013JC009187.

Smetacek, V., Passow, U., 1990. Spring bloom initiation and Sverdrup's critical-depth model. Limnol. Oceanogr. 35 (228–234), 1990. https://doi.org/10.4319/lo.1990.35.1.0228.

Sommer, U., Charalampous, E., Scotti, M., Moustaka-Gouni, M., 2018. Big fish eat small fish: implications for food chain length? Community Ecology Community Ecology 192, 107–115. https://doi.org/10.1556/168.2018.19.2.2.

Sonnewald, M., Dutkiewicz, S., Hill, C., Forget, G., 2020. Elucidating ecological complexity: Unsupervised learning determines global marine eco-provinces. Sci. Adv. 6, eaay4740 https://doi.org/10.1126/sciadv.aay4740.

Soppa, M.A., Völker, C., Bracher, A., 2016. Diatom phenology in the southern Ocean: Mean patterns, trends and the role of climate oscillations. Remote Sens. (Basel) 8, 420. https://doi.org/10.3390/rs8050420.

Stabeno, P.J., Schumacher, J.D., Ohtani, K. 1999. The Physical Oceanography of the Bering Sea. In: Loughlin, T.R., Ohtani, K. (eds.), Dynamics of the Bering Sea. University of Alaska Sea Grant, AK-SG-99-03, Fairbanks, ISBN: 1-56612-062-4.

Strom, S.L., Welschmeyer, N.A., 1991. Pigment-specific rates of phytoplankton growth and microzooplankton grazing in the open subarctic Pacific Ocean. Limnol. Oceanogr. 36 (50–63), 1991. https://doi.org/10.4319/lo.1991.36.1.0050.

Strom, S.L., Olson, M.B., Macri, E.L., Mordy, C.W., 2006. Cross-shelf gradients in phytoplankton community structure, nutrient utilization, and growth rate in the coastal Gulf of Alaska. Mar. Ecol. Prog. Ser. 328, 75–92.

Suchy, K.D., Young, K., Galbraith, M., Perry, R.I., Costa, M., 2022. Match/mismatch between phytoplankton and crustacean zooplankton phenology in the Strait of Georgia, Canada. Front. Mar. Sci. 9, 832684 https://doi.org/10.3389/fmars.2022.832684.

Suga, T., Motoki, K., Aoki, Y., Macdonald, A.M., 2004. The North Pacific climatology of winter mixed layer and mode waters. J. Phys. Oceanogr. 34, 3–22. https://doi.org/10.1175/1520-04852004034<0003:TNPCOW>2.0.CO;2.

Sugie, K., Kuma, K., Fujita, S., Nakayama, Y., Ikeda, T., 2010. Nutrient and diatom dynamics during late winter and spring in the Oyashio region of the western subarctic Pacific Ocean. Deep Sea Res. Part II 5717–18, 1630–1642. https://doi.org/10.1016/j.dsr2.2010.03.007.

Suzuki, K., Liu, H., Saino, T., 2002a. East–west gradients in the photosynthetic potential of phytoplankton and iron concentration in the subarctic Pacific Ocean during early summer. Limnol. Oceanogr. 476, 1581–1594. https://doi.org/10.4319/lo.2002.47.6.1581.

Suzuki, K., Minami, C., Liu, H., Saino, T., 2002b. Temporal and spatial patterns of chemotaxonomic algal pigments in the subarctic Pacific and the Bering Sea during the early summer of 1999. Deep-Sea Res. II 49, 5685–5704.

Suzuki, K., Hinuma, A., Saito, H., Kiyosawa, H., Liu, H., Saino, T., Tsuda, A., 2005. Responses of phytoplankton and heterotrophic bacteria in the northwest subarctic Pacific to in situ iron fertilization as estimated by HPLC pigment analysis and flow cytometry. Prog. Oceanogr. 64, 167–187.

Takeda, S., 2011. Iron and phytoplankton growth in the subarctic North Pacific. Aqua BioSci. Monogr. 4, 41–93. https://doi.org/10.5047/absm.2011.00402.0041.

Tsuda, A., Takeda, S., Saito, H., Nishioka, J., Kudo, I., Nojiri, Y., Suzuki, K., Uematsu, M., Wells, M.L., Tsumune, D., Yoshimura, T., aono, T., Aramaki, T., Cochlan, W.P., Hayakawa, M., Imai, K., Isada, T., Iwamoto, Y., Johnson, W.K., Kameyama, S., Kato, S., Kiyosawa, H., Kondo, Y., Levasseur, M., Machida, R.J., Nagao, I., Nakagawa, F., Nakanishi, T., Nakatsuka, S., Narita, A., Noiri, Y., Obata, H., Ogawa, H., Oguma, K., Ono, T., Sakuragi, T., Sasakawa, M., Sato, M., Shimamoto, A., Takata, H., Trick, C.G., Watanabe, Y.W., Wong, C.S., Yoshie, N. 2007. Evidence for the grazing hypothesis: Grazing reduces phytoplankton responses of the HNLC ecosystem to iron enrichment in the western subarctic Ppacific (SEEDS II). Journal of Oceanography, 63, 983–994, doi: 10.1007/s10872-007-0082-x.

Ueno, H., Bracco, A., Barth, J.A., Budyansky, M.V., Hasegawa, D., Itoh, S., Kim, S.Y., Ladd, C., Lin, X., Park, Y.-G., Prants, S., Ross, T., Rypina, I.I., Sasai, Y., Trusenkova, O.O., Ustinova, E.I., Zhong, Y., 2023. Review of oceanic mesoscale processes in the North Pacific: Physical and biogeochemical impacts. Prog. Oceanogr. 212, 102955 https://doi.org/10.1016/j.pocean.2022.102955.

Uitz, J., Claustre, H., Morel, A., Hooker, S.B., 2006. Vertical distribution of phytoplankton communities in open ocean: An assessment based on surface chlorophyll. J. Geophys. Res. 111, C08005. https://doi.org/10.1029/2005JC003207.

Unesco, 2009. Global Open Oceans and Deep Seabed GOODS – Biogeographic Classification. UNESCO-IOC., IOC Technical Series, Paris, p. 84.

Vesanto, J., Alhoniemi, E., 2000. Clustering of the self-organizing map. IEEE Trans. Neural Netw. 113, 586–600.

Vidussi, F., Claustre, H., Manca, B.B., Luchetta, A., Marty, J., 2001. Phytoplankton pigment distribution in relation to upper thermocline circulation in the eastern Mediterranean Sea during winter. J. Geophys. Res. 106 (C9), 19939–19956.

Vishnu, P.S., Costa, M., 2023. Evaluating the performance of Sentinel-3A OLCI products in the Subarctic Northeast Pacific. Remote Sens. (Basel) 15 (13), 3244. https://doi.org/10.3390/rs15133244.

Vishnu, P.S., Xi, H., Belluz, J.D.B., Hussain, M.S., Bracher, A., Costa, M., 2022. Seasonal dynamics of major phytoplankton functional types in the coastal waters of the west coast of Canada derived from OLCI Sentinel 3A. Front. Mar. Sci. 9, 1018510. https://doi.org/10.3389/fmars.2022.1018510.

Waga, H., Fujiwara, A., Hirawake, T., Suzuki, K., Yoshida, K., Abe, H., Nomura, D., 2022. Primary productivity and phytoplankton community structure in surface waters of the western subarctic Pacific and the Bering Sea during summer with reference to bloom stages. Prog. Oceanogr. 201, 102738 https://doi.org/10.1016/j.pocean.2021.102738.

Waite, J.N., Mueter, F.J., 2013. Spatial and temporal variability of chlorophyll-a concentrations in the coastal Gulf of Alaska, 1998–2011, using cloud-free reconstructions of SeaWiFS and MODIS-Aqua data. Prog. Oceanogr. 116, 179–192. https://doi.org/10.1016/j.pocean.2013.07.006.

Wang, X., Jiang, S., Wu, Y., Wang, Y., 2022. Synchronous shifts in nutrients and organic carbon responses over the diatom-to-dinoflagellate succession. Front. Mar. Sci. 9, 845372 https://doi.org/10.3389/fmars.2022.845372.

Wehrens, R., Buydens, L.M.C., 2007. Self- and super-organizing maps in R: The kohonen package. J. Stat. Softw. 215 https://doi.org/10.18637/jss.v021.i05.

Welch, H., Brodie, S., Jacox, M.G., Robinson, D., Wilson, C., Bograd, S.J., Oliver, M.J., Hazen, E.L., 2020. Considerations for transferring an operational dynamic ocean

management tool between ocean color products. Remote Sens. Environ. 242, 111753 https://doi.org/10.1016/j.rse.2020.111753.
Werdell, P.J., Bailey, S.W., Fargion, G.S., Pietras, C., Knobelspiesse, K.D., Feldman, G.C., McClain, C.R., 2003. Unique data repository facilitates ocean color satellite validation. EOS Trans. AGU 84 (38), 377.
Whitney, F.A., Crawford, W.R., Harrison, P.J., 2005. Physical processes that enhance nutrient transport and primary productivity in the coastal and open ocean of the subarctic NE Pacific. Deep-Sea Res. II 52, 681–706. https://doi.org/10.1016/j.dsr2.2004.12.023.
Wickham, H., 2016. ggplot2: Elegant Graphics for Data Analysis. Springer-Verlag, New York https://ggplot2.tidyverse.org.
Wickham, H., Averick, M., Bryan, J., Chang, W., McGowan, L.D., François, R., Grolemund, G., Hayes, A., Henry, L., Hester, J., Kuhn, M., Pedersen, T.L., Miller, E., Bache, S.M., Müller, K., Ooms, J., Robinson, D., Seidel, D.P., Spinu, V., Takahashi, K., Vaughan, D., Wilke, C., Woo, K., Yutani, H., 2019. Welcome to the tidyverse. Journal of Open Source Software 443, 1686. https://doi.org/10.21105/joss.01686.
Wilson, C., Coles, V.J., 2005. Global climatological relationships between satellite biological and physical observations and upper ocean properties. J. Geophys. Res. 110, C10001. https://doi.org/10.1029/2004JC002724.
Wong, T.T., 2015. Performance evaluation of classification algorithms by k-fold and leave-one-out cross validation. Pattern Recogn. 48, 2839–2846. https://doi.org/10.1016/j.patcog.2015.03.009.
Wright, S.W., Jeffrey, S.W., 2005. Pigment Markers for Phytoplankton Production. In: Volkman, J.K. (Ed.), Marine Organic Matter: Biomarkers, Isotopes and DNA. the Handbook of Environmental Chemistry, vol 2N. Springer, Berlin, Heidelberg. https://doi.org/10.1007/698_2_003.
Wright, S.W., Jeffrey, S.W., Mantoura, R.F.C., Llewellyn, C.A., Bjørnland, T., Repeta, D., Welschmeyer, N., 1991. Improved HPLC method for the analysis of chlorophylls and carotenoids from marine phytoplankton. Mar. Ecol. Prog. Ser. 77 (2/3), 183–196.
Xi, H., Losa, S.N., Mangin, A., Soppa, M.A., Garnesson, P., Demaria, J., Liu, Y., d'Andon, O.H.F., Bracher, A., 2020. Global retrieval of phytoplankton functional types based on empirical orthogonal functions using CMEMS GlobColour merged products and further extension to OLCI data. Remote Sens. Environ. 240, 111704 https://doi.org/10.1016/j.rse.2020.111704.
Xi, H., Losa, S.N., Mangin, A., Garnesson, P., Bretagnon, M., Demaria, J., Soppa, M.A., d'Andon, O.H.F., Bracher, A., 2021. Global chlorophyll a concentrations of phytoplankton functional types with detailed uncertainty assessment using multisensor ocean color and sea surface temperature satellite products. J. Geophys. Res. Oceans 126. https://doi.org/10.1029/2020JC017127 e2020JC017127.
Yasuda, I., Kouketsu, S., Katsumata, K., Ohiwa, M., Kawasaki, Y., Kusaka, A., 2002. Influence of Okhotsk Sea Intermediate Water on the Oyashio and North Pacific Intermediate Water. J. Geophys. Res. 107C12, 3237. https://doi.org/10.1029/2001JC001037.
Yatsu, A., Chiba, S., Yamanaka, Y., Ito, S.-I., Shimizu, Y., Kaeriyama, M., Watanabe, Y., 2013. Climate forcing and the Kuroshio/Oyashio ecosystem. ICES J. Mar. Sci. 70, 922–933. https://doi.org/10.1093/icesjms/fst084.
Yoo, S., Batchelder, H.P., Peterson, W.T., Sydeman, W.J., 2008. Seasonal, interannual and event scale variation in North Pacific ecosystems. Prog. Oceanogr. 77, 155–181. https://doi.org/10.1016/j.pocean.2008.03.013.
Zapata, M., 2005. Recent advances in pigment analysis as applied to picophytoplankton. Vie Milieu 55, 233–248.
Zhang, Y., Jiao, N., Hong, N., 2008. Comparative study of picoplankton biomass and community structure in different provinces from subarctic to subtropical oceans. Deep-Sea Res. II 55, 1605–1614. https://doi.org/10.1016/j.dsr2.2008.04.014.
Zhang, H.-R., Yuntao, W., Peng, X., Fei, C., 2021. Modeling the seasonal variability of phytoplankton in the subarctic Northeast Pacific Ocean. Mar. Ecol. Prog. Ser. 680, 33–50. https://doi.org/10.3354/meps13914.